

## An aftershock study of the El Asnam (Algeria) earthquake of 1980 October 10

**M. Ouyed** *Laboratoire de Geophysique Interne, IRIGM, Universite Scientifique et Medicale de Grenoble, BP No. 53X, 38041 Grenoble Cedex, France and Centre National d'Astronomie, d'Astrophysique et de Geophysique, BP 15–16, Algiers Bouzareah, Algeria*

**G. Yielding** *Bullard Laboratories, Department of Earth Sciences, University of Cambridge, Madingley Rise, Madingley Road, Cambridge CB3 0EZ*

**D. Hatzfeld** *Laboratoire de Geophysique Interne, IRIGM, Universite Scientifique et Medicale de Grenoble, BP No. 53X, 38041 Grenoble Cedex, France*

**G. C. P. King** *Bullard Laboratories, Department of Earth Sciences, University of Cambridge, Madingley Rise, Madingley Road, Cambridge CB3 0EZ*

Received 1982 November 15; in original form 1982 May 14

**Summary.** An array of 28 portable seismic stations was operated in the region of El Asnam following the magnitude 7.3 ( $M_s$ ) thrust earthquake of 1980 October 10. Locations of 494 events are presented in this paper and provide an indication of the overall form of the aftershock distribution. Tests to establish location accuracy (particularly depth) reduce this set to 277 events which, it is argued, are well constrained. *P*-waves alone are used in this study as a consequence of a debate about the reliability of reading *S*-phases. From the reduced set of 277 events, 81 events provide well-constrained focal mechanisms.

The locations are presented in the form of maps and cross-sections, and discussed in relation to information already derived from field mapping of surface breaks and teleseismic studies of the waveforms of the main event. The zone of surface faulting (including secondary normal faulting) extended for 35 km but the aftershock distribution extends for twice this distance. Along the part of the fault which experienced substantial displacement in the main shock, the fault plane itself appears to be devoid of aftershocks, although many lie in the footwall beneath the fault. At junctions between segments of thrust faulting, strike-slip motion occurs. This is apparent in the aftershock focal mechanisms, and in the surface ruptures in one place.

The large number of aftershocks in the north-east area appears to be due to the reactivation of a fan-like system of smaller reverse faults associated with surface folding. Activity at the south-west end is considerably less than that in the north-east, and is not obviously associated with recognizable geological or morphological features.

## 1 Introduction

The El Asnam (Algeria) earthquake occurred at 12.25 GMT 1980 October 10, and had a surface-wave magnitude of 7.3 (USGS). It was one of the largest earthquakes in the Mediterranean region in recent years, and the largest ever instrumentally recorded in the Atlas belt of north-west Africa. Immediately following the main shock, scientists from a number of countries began studies in the epicentral region. Results published so far include descriptions of the surface faulting and its structural setting, relocation of the main shock and major aftershocks, focal mechanism and waveform modelling of the main shock, and preliminary locations of locally recorded aftershocks (Ouyed *et al.* 1980, 1981; Lepvrier 1981; King & Vita-Finzi 1981; Ambraseys 1981; Yielding *et al.* 1981). This paper presents locations for almost 500 locally recorded aftershocks, and more than 80 individual focal mechanisms. These results are used to interpret the tectonic environment of the aftershock sequence.

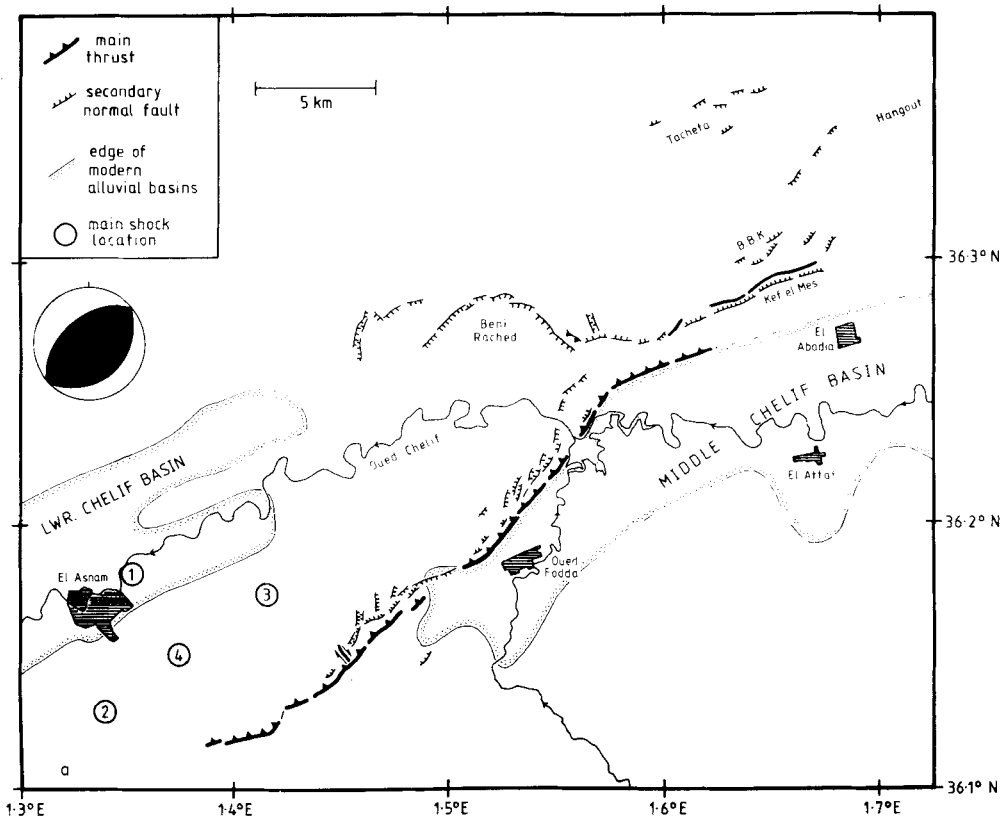


**Figure 1.** (a) Simplified map of the surface breaks produced by the El Asnam earthquake of 1980 October 10, based on Philip & Meghraoui (1983) and Yielding *et al.* (1981). The fault on Kef el Mes (marked as a bold line) is interpreted differently: Philip & Meghraoui interpret it as a normal fault which curves at shallow depths to become the main thrust fault (northern segment); Yielding *et al.* interpret it as a normal fault caused by bedding-plane slip in the hanging-wall of the main fault (northern segment). The focal mechanism of the main shock (after Ouyed *et al.* 1981) is shown, and also the location of the main shock by different authors: (1) USGS; (2) CSEM; (3) Cisternas *et al.* (1982); (4) Yielding *et al.* (1981). The lake which formed soon after the earthquake is shown stippled. (b) Topographic map of the same area as (a).

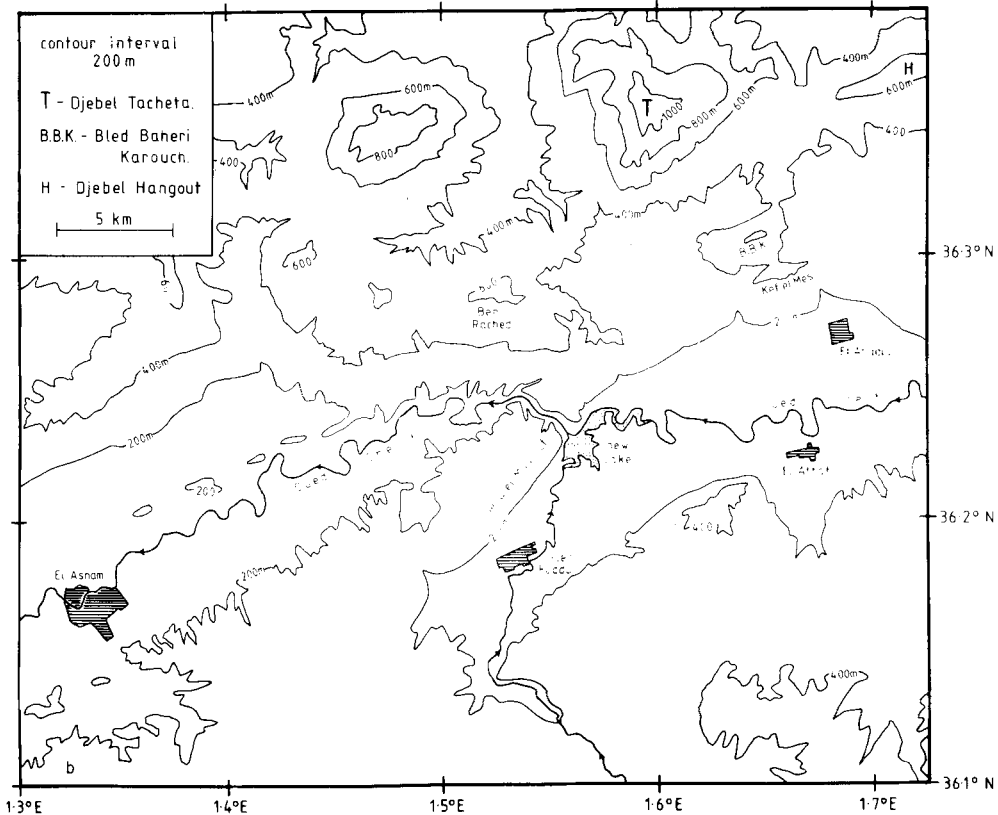


Figure 1 – continued

The main shock of 1980 October 10 occurred between the lower and Middle Chelif Basins, on a NE-striking reverse fault which dips NW beneath a range of low hills (see Fig. 1). Surface ruptures on the reverse fault extended for 30 km, with an average displacement of 2–3 m. Major offsets and changes of trend divide the reverse fault into southern, central and northern segments; the southern and central segments were each about 12 km long, the northern segment only 5 km. In addition to the reverse faulting, a large amount of normal faulting was also observed at the surface. Much of this was caused by tension on anticlines whose amplitude increased during the earthquake as a consequence of motion at depth on the main and related faults (King & Vita-Finzi 1981). A large arcuate system of faults in the Beni Rached area (see Fig. 1) is less well understood and has been interpreted as a tensional mechanism similar to elsewhere (Yielding *et al.* 1981; Cisternas, Dorel & Gaulon 1982) or as a landslide (Ouyed *et al.* 1981; Ambraseys 1981; Yielding *et al.* 1981).

Epicentral locations for the main shock, by various authors (see Fig. 1), suggest that the rupture initiated near the south-west end of the observed reverse fault, near the city of El Asnam. The depth of the focus has been calculated as  $10 \pm 2$  km using waveform modelling (Yielding *et al.* 1981). The focal mechanism (see Fig. 1) is well constrained with a dip of  $52\text{--}58^\circ$  for the NW-dipping nodal plane which the surface fault break indicates is the fault plane. Major aftershocks (occurring within a few hours of the main shock) were predominantly NE of the main shock, near the central and northern fault segments (Ouyed *et al.* 1981; Yielding *et al.* 1981; Ouyed 1981). The largest aftershock (15.39 GMT, 1980 October 10,  $m_b = 6.3$ ) may have contributed to the observed displacement on the central fault segment.

Three studies have been published of waveform modelling of long-period seismograms at various WWSSN stations. Ouyed *et al.* (1981) used a single point source, with a trapezoidal time function of total duration 12 s. This produces a good general fit to the first part of the observed seismograms. However, at some stations a secondary arrival is observed about 3–4 s after the first one. Yielding *et al.* (1981) showed that this could be modelled by means of a double rupture, the second source being 12 km NE of the first and occurring 4 s later. Such a separation agrees well with the observed spacing of the southern and central segments of the fault break (with rupture initiation occurring at the SW end). Furthermore, the second source is required to have a fault-plane of shallower dip ( $45^\circ$ ). This suggests that the dip of the central segment of the fault is shallower than that of the southern segment. Subsequent work (Deschamps, Gaudemer & Cisternas 1982) suggests that the northern segment may have been the site of a later third rupture.

## 2 Operation of array, and data reduction

The first portable seismic stations were installed in the epicentral area within 48 hr of the main shock. These were progressively augmented to give a maximum array of 28 stations (22 smoked-drum recorders with vertical-component seismometers, and six 3-component analogue magnetic tape recorders). Fig. 2 shows the distribution of stations, and Table 1 lists the type and operating period of each station. Because of the high level of seismicity (over 80 shocks of  $M > 2$  per day), instruments were operated at relatively low gains and noise levels were not a problem.

The smoked-drum recorders were all MEQ-800 instruments, except for the stations DAM, BDA and BDB which were Lamont 'big-drum' instruments. The recorders were run with a drum-speed of 60 or 120 mm min<sup>-1</sup>, and hour-, minute- and second-marks were written on the records by an internal quartz clock. Clock drifts were generally less than 0.05 s day<sup>-1</sup>, and were calibrated against radio time signals (usually the Swiss station

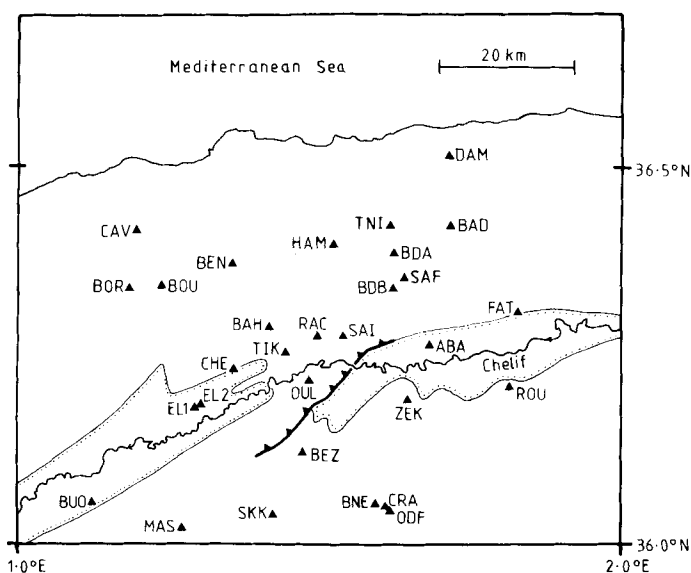


**Figure 2.** Map showing the locations of the seismic stations used for this study. The dotted line shows the edge of the Chelif alluvial basins. The barbed line shows the trace of the 1980 surface break.

Table 1. Station list.

Station	Provenance	Type	Period of Operation	Comments
SAF	IPGP/SPGM	Smoked-drum	12/10 - 16/11	
OUL	"	"	"	
CRA	"	"	"	
MAS	"	"	"	
CAV	"	"	13/10 - 28/10	moved to ROU
ROU	"	"	28/10 - 16/11	
ZEK	"	"	15/10 - 16/11	
BEN	"	"	"	
EL1	"	"	15/10 - 17/10	moved to EL2
EL2	"	"	17/10 - 16/11	
TNI	"	"	15/10 - 16/11	
BOU	"	"	16/10 - 16/11	
SKK	"	"	"	
BEZ	IPGP	Magnetic	"	
CHE	"	"	"	
TIK	"	"	16/10 - 21/10	moved to RAC
RAC	"	"	21/10 - 16/11	
OLD	CEA	"	21/10 - 25/11	
ODF	"	"	"	
ABA	"	"	22/10 - 25/11	
FAT	U.Camb.	Smoked-drum	22/10 - 16/11	
HAM	"	"	23/10 - 16/11	
BNS	"	"	"	
RUO	"	"	23/10 - 14/11	
SAI	"	"	24/10 - 16/11	
BAH	"	"	"	
BOR	"	"	25/10 - 16/11	
BAD	"	"	26/10 - 14/11	
BDB	"	"	7/11 - 15/11	
BDA	"	"	10/11 - 15/11	
DAM	"	"	10/11 - 14/11	

IPGP = Institut du Physique du Globe, Paris, France.  
 SPGM = Service du Physique du Globe, Rabat, Morocco.  
 CEA = Commissariat a l'Energie Atomique, Paris, France.  
 U.Camb. = University of Cambridge, England.

HBG) every 24 or 48 hr. Time corrections were added to arrival times by linearly interpolating between calibration times. *P*-arrivals could be read to within 0.1 mm using a graduated magnifying glass, corresponding to 0.1 s for a 60 mm min<sup>-1</sup> drum speed or 0.05 s for a 120 mm min<sup>-1</sup> drum speed. Additional error from interpolation of clock drift was estimated at 0.02 s. Part of a typical smoked-drum record is shown in Fig. 3.

For the magnetic-recording stations, radio time-marks were written directly on to the magnetic tape, removing the need for an internal clock. The precision of reading arrival times was in this case dependent upon the playback speed used, and was estimated to be about 0.03 s.

The locations presented in this paper are for the larger events of the aftershock series between 1980 October 15 and 1980 November 16. These events were chosen by visual inspection of the records. The location program *HYPOLINVERSE* (Klein 1978) was used for initial testing of velocity models, etc. but the *HYP071* program (Lee & Lahr 1975) was used for the final runs.

Magnitudes were calculated from signal duration by the method of Adams (1977), using the formula

$$M = a(\log T) - b$$

where *T* is signal duration, and *a* and *b* are constants which were calculated for each station. Larger events (*M* > 4), recorded teleseismically, were used to calculate *a* and *b* at a reference station (OUL), and magnitudes at OUL were then used to calculate *a* and *b* at all other stations. The final magnitude cited for any event is the mean of the magnitudes calculated at the different stations. The quoted magnitudes are only approximate (to about 0.5) and relative.

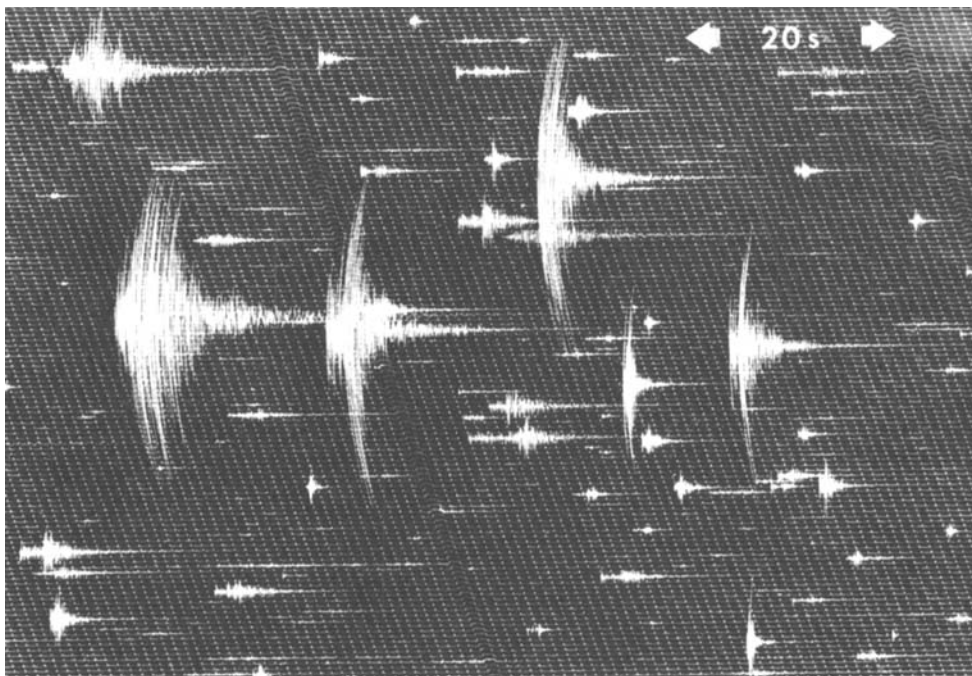


Figure 3. Part of a typical smoked-drum record, recorded at station ZEK on 1980 October 29–30.

### 3 Use of *S*-phases in earthquake location

Many studies (e.g. James *et al.* 1969; Buland 1976; Soufleris *et al.* 1982; Ellsworth & Roecker 1983) have demonstrated that the accuracy of earthquake location is greatly improved if *S*-phases are used in addition to *P*. In particular, the use of *S*-arrivals gives some constraint on the origin time of the earthquake, and therefore restricts the trade-off between origin time and depth which can occur when only *P*-arrivals are used; hence the depth of the earthquake is better resolved. Thus the use of both *P*- and *S*-arrivals in earthquake location is to be preferred whenever possible.

However, for aftershocks recorded on the portable instruments in the El Asnam area, *S*-arrivals often had a strongly emergent character and are therefore difficult to read accurately. In addition, records from the three-component seismic stations installed by IPG, Paris show secondary phases which sometimes arrive at different times in the horizontal and vertical components (Sapin, Wittlinger & Hirn 1983). In some cases the arrival is earlier on the horizontal component than on the vertical, whereas in some cases it is earlier on the vertical component. It is not yet clear which component is more reliable. In this study only *P*-arrivals have been used; relocations using both *P*- and *S*-arrivals will be the subject of a subsequent paper.

### 4 Choice of velocity model; location errors

Prior to the El Asnam 1980 earthquake, no detailed investigation of the velocity structure of the Tellian Atlas had been performed, though Bockel (1972) obtained a value of  $5.55 \text{ km s}^{-1}$  for  $P_g$  waves on the basis of arrival times of local earthquakes recorded at permanent seismic observatories. Geological studies (e.g. Perrodon 1957; Mattauer 1963) show that the present

**Table 2.** Synthetic earthquake tests.

Model	V1 (km/s)	V2 (km/s)	Range of RYS (s)	Range of ERH (km)	Range of epicentral mislocation (km)	Range of ERZ (km) (*)	Range of depth mislocation (km)
1.	5.0	6.0	-	-	-	-	-
2.	4.5	6.0	0-0.06	0-0.2	0-0.4	0-0.1*	-0.1 to +1.0
3.	5.5	6.0	0-0.05	0-0.3	0-0.4	0-0.4	-0.4 to +0.6
4.	5.0	5.5	0.03-0.16	0.1-1.1	0.1-1.1	0.3-1.5	+1.2 to +7.3
5.	5.0	6.5	0.03-0.11	0.1-1.1	0.1-1.4	0.2-1.7*	-0.8 to -5.7
1N.	5.0	6.0	0.05-0.11	0.2-0.7	0-1.4	0.4-1.1	-1.7 to +1.5
2N.	4.5	6.0	0.05-0.12	0.2-0.7	0.1-1.8	0.3-1.1*	-1.4 to +1.9
3N.	5.5	6.0	0.05-0.11	0.2-0.7	0.1-1.4	0.4-1.1	-2.2 to +1.1

V1 and V2 are velocities in upper and lower layers. (In all models, layer 1 is 3 km thick.)

Travel times for synthetic earthquakes were calculated using model 1. These events were relocated in various other velocity models (2–5) to examine the effect of incorrect velocity model on location error. For models 1N, 2N, 3N, random noise of 0.1 s standard deviation was added to the arrival-time data before relocation. ‘Epicentral mislocation’ is the distance between real and relocated epicentres. ‘Depth mislocation’ is the relocated depth minus the real depth.

\*Three unstable locations (having ERZ 72.7, 146.5 and 110.9 km) have been ignored in this column.

alluvial plains of the Chelif valley are remnants of a more extensive Miocene basin. This basin contains sediments (mostly marls and sands) which may be up to 4 km thick under the modern Chelif River. The sediments thin to the north and south, exposing the pre-Miocene rocks which are comprised of flysch, marls and limestones, arranged in a sequence of nappes (Mattauer 1963).

As a first approximation to the known geological structure, the velocity structure of the upper crust can be expected to be a thin layer of low velocity (representing the basal sediments) overlying a layer of higher velocity (representing the pre-Miocene rocks). Five different models of this type were used to locate six well-recorded earthquakes (> 20 stations). These tests suggested that a velocity model having an upper layer of 5 km s<sup>-1</sup> and 3 km thick, overlying a 6 km s<sup>-1</sup> half-space, produced a good fit to the observed arrival times. To explore further the applicability of this model, relocations were performed using synthetic earthquake data. The synthetic events were positioned at six places throughout the area of the array, with focal depths of 1, 7 and 13 km. Travel times were calculated to a representative selection of stations, using the velocity model described above. These theoretical travel times were then used to relocate the synthetic earthquakes in a variety of velocity models. The results are summarized in Table 2.

The different velocity models all produce very similar epicentral locations, always within 1.5 km of the real epicentre. Changing the velocity of the upper layer from 5 to 4.5 or 5.5 km s<sup>-1</sup> produces similar small changes in depths (less than 1 km). However, changing the

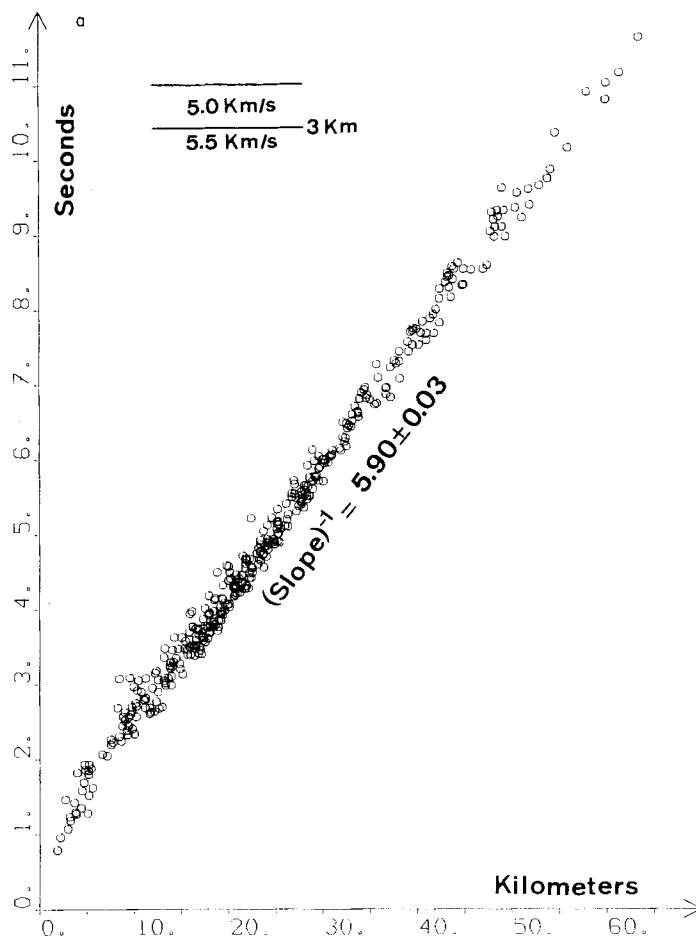


**Figure 4.** Plots of travel-times against epicentral distance for selected earthquakes ( $>20$  stations,  $\text{rms} < 0.1$  s, depth  $< 5$  km), using three different velocity models. Note that plot (b) shows the smallest scatter of arrival times, suggesting that a half-space velocity of  $6.0 \text{ km s}^{-1}$  is a better choice than  $5.5 \text{ km s}^{-1}$  (a) or  $6.5 \text{ km s}^{-1}$  (c).

velocity of the underlying half-space has a more dramatic effect on the depths. Increasing the half-space velocity from  $6$  to  $6.5 \text{ km s}^{-1}$  produces depths shallower by  $0.8$ – $5.7$  km, whereas decreasing the velocity to  $5.5 \text{ km s}^{-1}$  produces depths greater by  $1.2$ – $7.3$  km. This is because, when only  $P$ -arrivals are used, the location program can adjust the origin time in addition to the depth, to fit the observed arrival times. It is noteworthy that the standard vertical error of location (ERZ) produced by the location program is commonly much smaller than the mislocation caused by an incorrect velocity model (see Table 2). Hence it is very important that the velocity model used should be as close as possible to the velocity structure in the aftershock zone.

To provide further constraint on the half-space velocity, real earthquakes were located using three different velocity models, and time–distance graphs were plotted (see Fig. 4). Of the three models, the scatter of points is smallest for an underlying half-space of  $6 \text{ km s}^{-1}$ , i.e. this model gives the smallest RMS of travel-time residuals. Using a half-space velocity of  $5.5 \text{ km s}^{-1}$  gives an apparent velocity on the travel-time graph of  $5.9 \text{ km s}^{-1}$  (Fig. 4a). On the other hand, the model with a half-space velocity of  $6.5 \text{ km s}^{-1}$  gives an apparent velocity of  $6.13 \text{ km s}^{-1}$  (Fig. 4c). This also suggests that the model with a half-



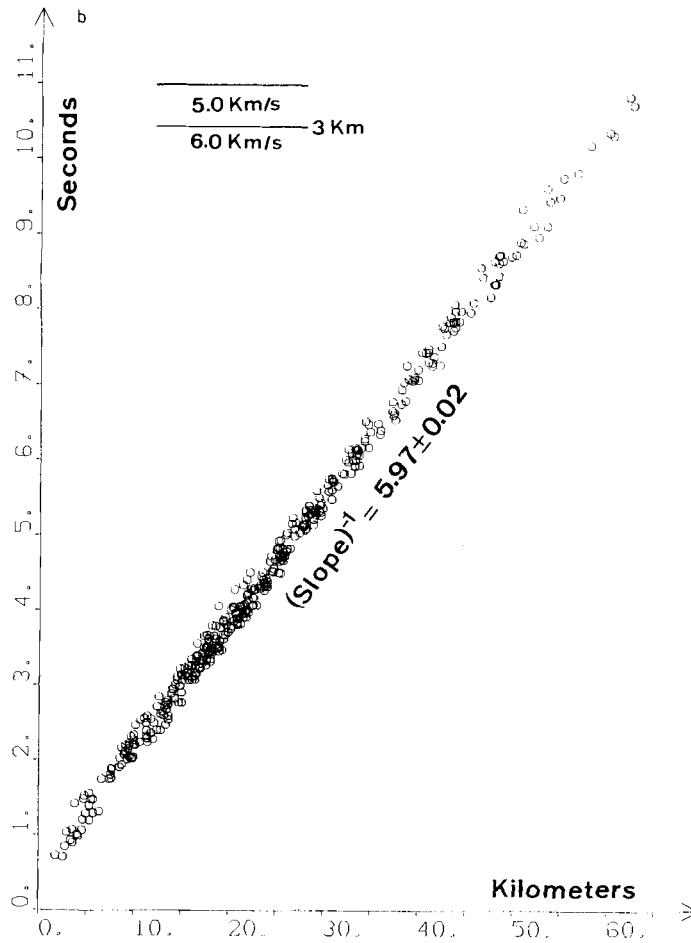


Figure 4 – continued

space velocity of  $6.0 \text{ km s}^{-1}$  is a better choice than  $5.5$  or  $6.5 \text{ km s}^{-1}$ . The depth errors for the final locations should therefore be much smaller than the errors obtained above in the synthetic tests, since we now have some constraint on the half-space velocity.

The real arrival-time data are contaminated with noise, since the reading accuracy of the records is of the order of  $0.1 \text{ s}$  (as discussed in a previous section). The effect of this on location accuracy was also examined using synthetic earthquake data, and the results are shown in Table 2. Addition of random noise (of  $0.1 \text{ s}$  standard deviation) to arrival-time data, followed by relocation in the initial velocity model, produced up to  $1.4 \text{ km}$  epicentral mislocation and  $\pm 1.7 \text{ km}$  error in depth (model 1N in Table 2). These mislocations are larger than the horizontal and vertical standard errors (ERH and ERZ) produced by the location program (ERH  $< 0.7 \text{ km}$ , ERZ  $< 1.1 \text{ km}$ ). Relocation in a different velocity model, in addition to having random noise, increases the depth mislocation up to  $2.2 \text{ km}$  (model 3N in Table 2).

From the foregoing tests we can draw the following conclusions about location accuracy:

- (1) Epicentral locations show little dependence on velocity model.
- (2) Location depths are strongly dependent on the value of the half-space velocity in the velocity model, but show little dependence on the velocity of the top layer in the model.

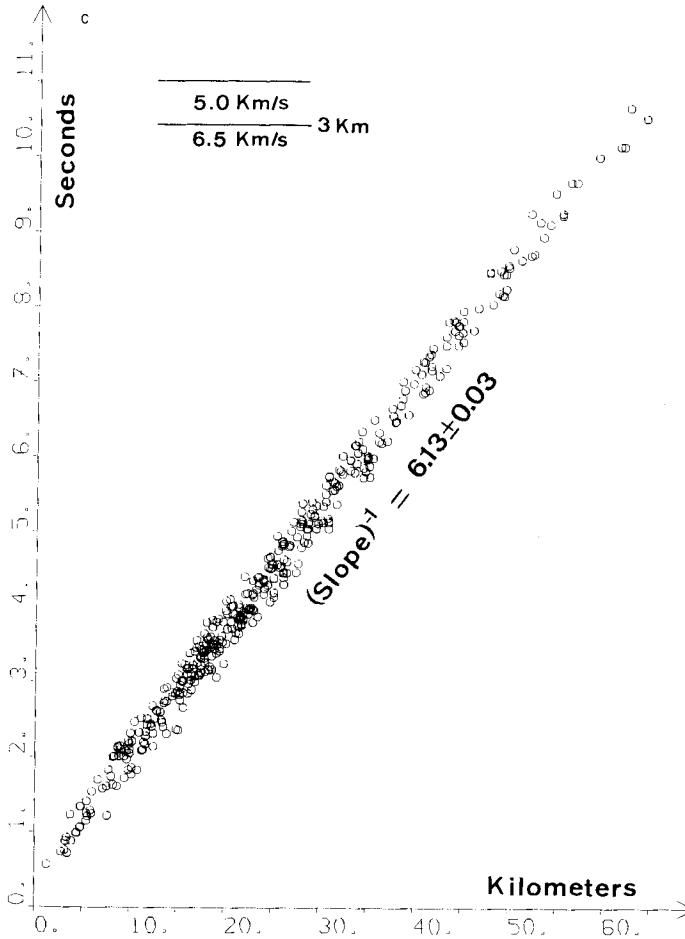


Figure 4 – continued

(3) A velocity for the underlying half-space of  $6 \text{ km s}^{-1}$  gives a better fit to the observed travel times than one of  $5.5 \text{ km s}^{-1}$  or one of  $6.5 \text{ km s}^{-1}$ . Constraint on this parameter in the velocity model removes the largest possible source of location error.

(4) When random noise of 0.1 s standard deviation is added to theoretical travel times, location errors of about  $\pm 2 \text{ km}$  can result. These errors may be twice as large as the standard errors quoted by the location program (ERH and ERZ).

The model chosen for all subsequent locations was model 1 of Table 2: upper layer of  $5 \text{ km s}^{-1}$  and 3 km thick, overlying a  $6 \text{ km s}^{-1}$  half-space. To correct for the different heights of the seismic stations (88–1060 m), a time correction was applied to the arrivals at each station. This correction was calculated by dividing the height of each station by a velocity of  $2.5 \text{ km s}^{-1}$  (assumed velocity for weathered surface rocks).

## 5 Epicentral locations

A total of 494 events have been located for the period 1980 October 15 to 1980 November 16 (5–37 days after the main shock). These are shown in Fig. 5, which also shows the distribution of surface breaks caused by the main shock. In order to study the pattern of defor-

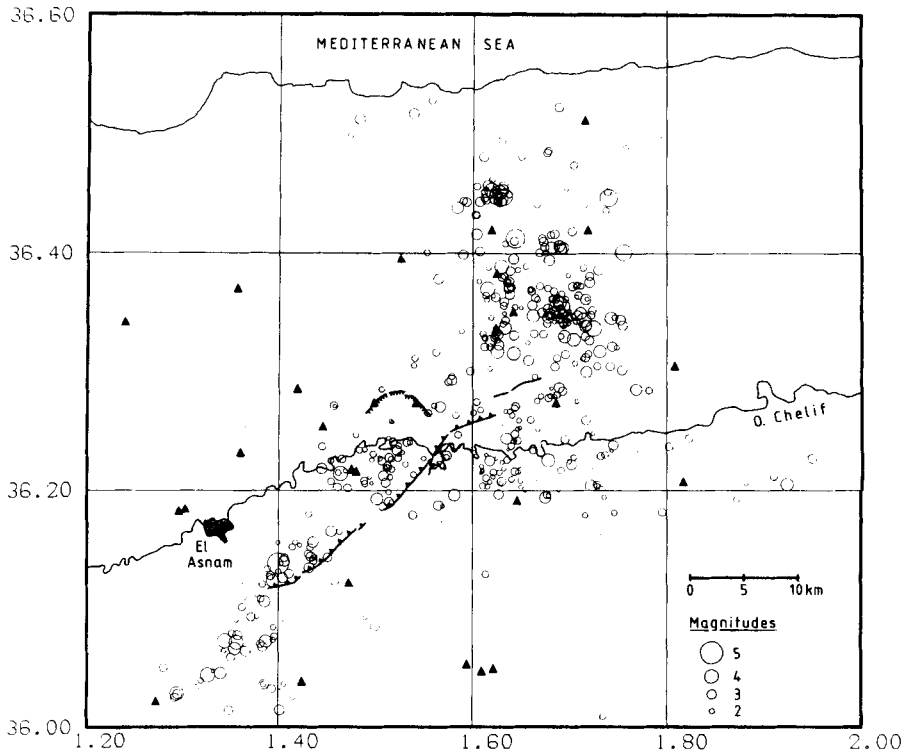


**Figure 5.** Map of the 494 aftershocks located between 1980 October 15 and November 16. Seismic stations are shown as triangles. The surface trace of the main thrust fault is shown as a barbed line (simplified from Fig. 1a).

mation in detail, it is important that only high quality locations are considered. To select such locations, the following criteria were used:

- (1) RMS of residuals less than 0.15 s;
- (2) ERH ('standard horizontal error') less than 2 km;
- (3) ERZ ('standard vertical error') less than 2 km;
- (4) at least one station lying at an epicentral distance less than twice the depth.

The fourth criterion ensures that shallow poorly resolved events are excluded. Events near the surface are always more poorly resolved than deeper events but resolution is improved in the vicinity of stations (Soufleris *et al.* 1982). It would be better to consider only those events within a distance equal to the depth, but because of the shallowness of the aftershocks relative to the station spacing this gives a distorted picture of the epicentral distribution, and therefore this criterion was relaxed. Applying the four quality criteria leaves 277 well-located events, which are shown in Fig. 6.

The general pattern of the seismicity is similar to that observed in preliminary studies by Ouyed *et al.* (1981) and Yielding *et al.* (1981). A number of important features may be noted:

- (1) The aftershock activity extends well beyond the ends of the main shock surface break. The length of the reverse fault surface breaks was about 30 km, whereas the aftershocks zone measures about 75 km NE–SW.

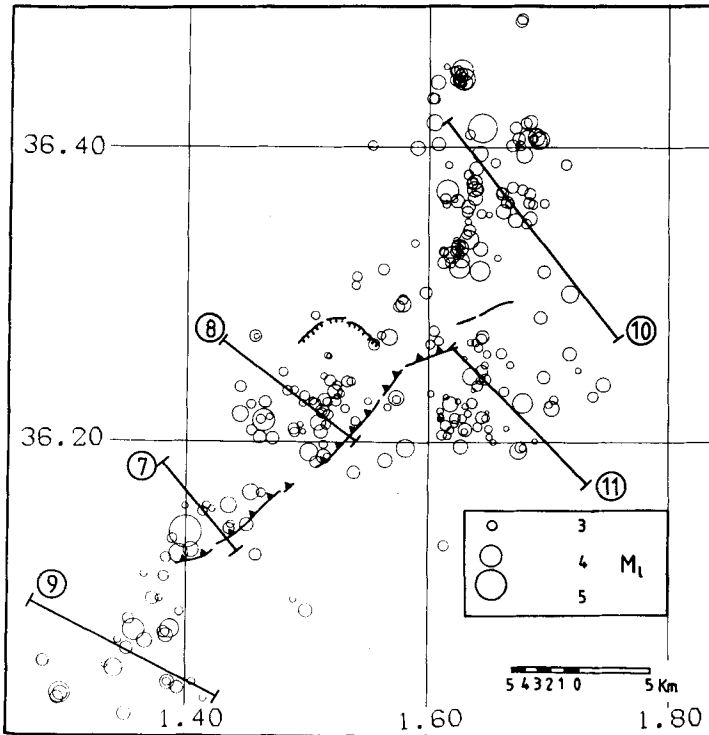


**Figure 6.** Map of the 277 locations which pass the following quality criteria:  $RMS < 0.15$  s, ERH,  $ERZ < 2$  km,  $D_{min} < 2 \times \text{depth}$  (see text). The surface trace of the main thrust fault is shown as a barbed line (simplified from Fig. 1a). The lines show the traces of the cross-sections in Figs 7–11.

(2) Clouds of seismicity are associated with both the southern and central segments of the main reverse fault which ruptured in the main shock. There is an apparent gap in the seismicity at the NE end of the southern segment, and also a lack of activity at the junction between the central segment and the northern segment.

(3) To the NE of the surface breaks there is a large spread of events. However, these are often localized into small groups. A temporal study of this activity (Ouyed 1981) shows that each of these groups is a discrete aftershock sequence occurring after a larger event (e.g. a magnitude 5 event at 23.38 GMT on 1980 October 30, and a magnitude 4.2 event at 02.06 GMT on 1980 November 8).

(4) The aftershock activity beyond the south-west end of the surface breaks is much less than that in the NE area.

(5) A scatter of events occurs in the Chelif valley, east of the thrust breaks.

(6) We have found very little seismicity in the Beni Rached area, where there was considerable normal faulting observed at the surface in both the 1980 earthquake (Fig. 1) and the 1954 earthquake (Rothé 1955).

## 6 Hypocentre locations

To examine the distribution of aftershocks with depth, the area was divided into segments, and a cross-section was taken across each segment, perpendicular to the local structural

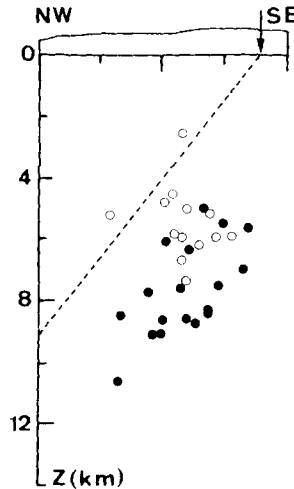


**Figure 7.** Cross-section of the southern segment of the fault (see Fig. 6 for location). The filled black dots represent aftershock locations which pass the quality criteria (see Fig. 6); open dots are other locations. The arrow shows the position of the surface break, and the dashed line shows the position of the main fault assuming a dip of  $52^\circ$  (from the focal mechanism in Fig. 1a). The surface topography is shown with a vertical exaggeration of  $\times 3$ .

trend. The segments considered were:

- (1) the southern segment of the main surface break;
- (2) the central segment of the surface break;
- (3) the area SW of the surface break;
- (4) the area NE of the surface break;
- (5) the Chelif valley (east of the surface break).

The locations of the cross-sections are shown on Fig. 6.

### 6.1 SOUTHERN SEGMENT OF FAULT-BREAK

A NW–SE cross-section is shown in Fig. 7. The locations lie in the depth range 5–11 km, and are no more than 5 km NW of the thrust break observed at the surface. The focal mechanism of the main shock (Fig. 1) gives a fault dip (to the NW) of about  $52^\circ$ ; waveform modelling of the main shock as a double rupture suggests a dip of about  $58^\circ$  for the fault along the southern segment (Yielding *et al.* 1981). These dip values imply that the aftershock locations are restricted to the footwall of the main fault along this segment. A small amount of surface faulting is seen in the footwall block of the southern segment (see Fig. 1a); however, this occurs on a minor NW-facing escarpment about 2 km from the main thrust, and its relationship to subsurface faulting is not clear.

### 6.2 CENTRAL SEGMENT OF THE FAULT-BREAK

A NW–SE cross-section is shown in Fig. 8. The general pattern is similar to that beneath the southern segment, but the locations extend further to the NW. If the dip of the main fault is  $50$ – $60^\circ$  here, as it appears to be further to the SW, then the aftershocks lie in both the footwall and hanging-wall of the fault. If, on the other hand, they are restricted to the footwall, as they appear to be to the SW, then the dip of the main fault along the central segment

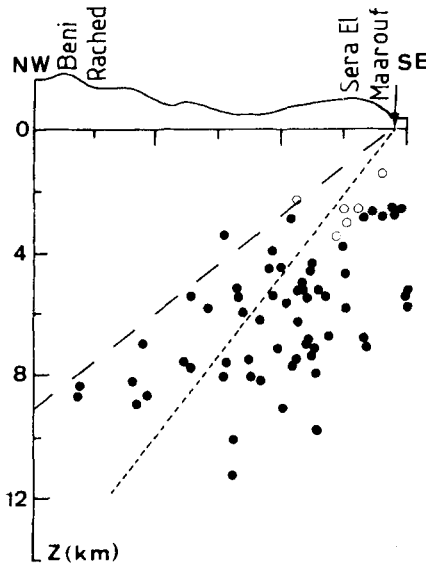


**Figure 8.** Cross-section of the central segment of the fault (see Fig. 6 for location). Notation as for Fig. 7, except that two possible fault dips are shown ( $40^\circ$  and  $52^\circ$ ).

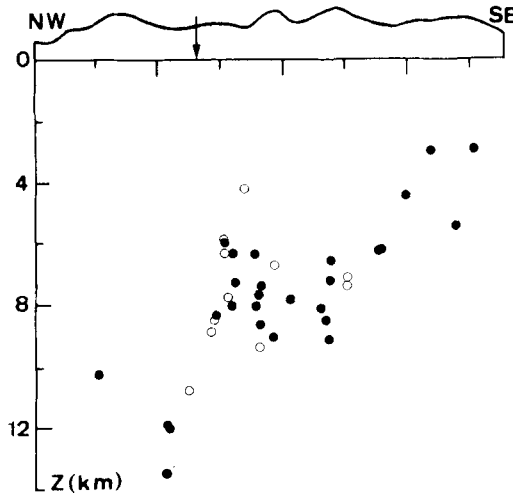


**Figure 9.** Cross-section of the area SW of the surface breaks (see Fig. 6 for location). The arrow shows the prolongation of the southern segment of the observed thrust fault. Other notation as in Fig. 7.

must be about  $40^\circ$ , i.e. shallower than along the southern segment. It may be significant that waveform modelling of the main shock (Yielding *et al.* 1981) suggests that the dip of the central segment is shallower than that of the southern segment. It is noteworthy that the events beneath Beni Rached are at 8–10 km depth and appear to be related to the main fault at depth (see Fig. 8). This lack of shallow activity beneath Beni Rached does not provide independent evidence that the Beni Rached surface breaks are of tectonic origin, rather than large-scale slumping.

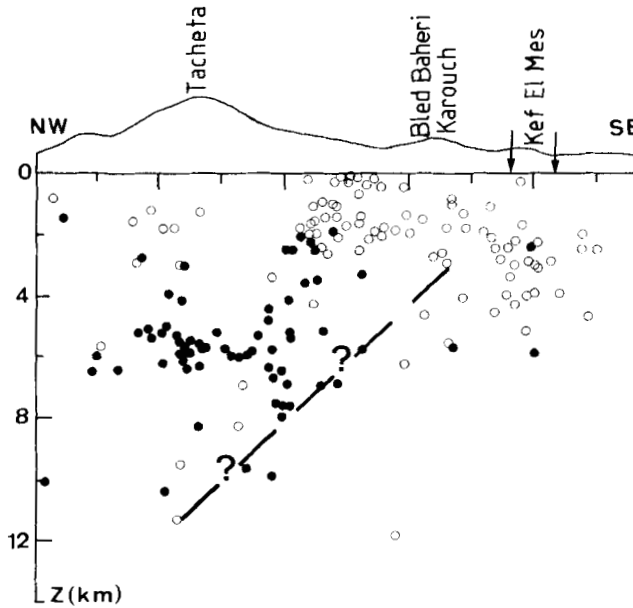


Figure 10. Cross-section of the north-eastern area (see Fig. 6 for location). The arrows show the positions of the northern segment of faulting, and the dashed line shows the probable position of the main thrust fault (northern segment).

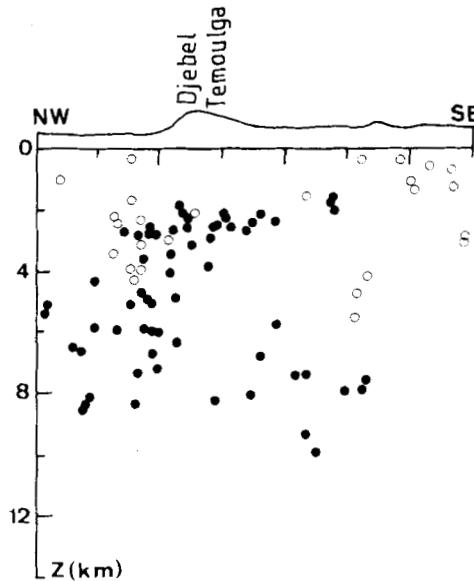


Figure 11. Cross-section of the eastern area (Chelif valley) (for location see Fig. 6). Notation as for Fig. 7.

### 6.3 SOUTH-WEST OF THE SURFACE BREAKS

The epicentral pattern in this area (see Fig. 6) is displaced to the south from the locations along the southern segment. Depths increase systematically from 3 km in the SE to 13 km in the NW, as is seen in a NW–SE cross-section (Fig. 9). The locations appear to define a

NW-dipping zone, parallel to the main fault but SE of it. It is possible that this zone represents another large fault segment, offset to the SE from that which ruptured in the main shock, but its projection up to the surface does not coincide with any known faults.

#### 6.4 NORTH-EASTERN AREA

The well-located events of the north-eastern area cluster into a few groups (see Fig. 6). A NW–SE cross-section is shown in Fig. 10. In contrast to the southern and central segments, aftershock activity is concentrated in the hanging-wall of the main fault (northern segment). However, the pattern of observed surface breaks and anticlines in this area suggests that a number of structures are active (Yielding *et al.* 1981), and hence the seismicity may not be directly related to the fault which ruptured in the main shock. In Fig. 10, many of the deeper events (4–8 km) occur beneath Djebel Tacheta, whereas most of the shallow events occur beneath Djebel Hangout (east of the line of section).

#### 6.5 EASTERN AREA (CHELIF VALLEY)

A NW–SE section is shown in Fig. 11. The apparently well-located events in this area range in depth from 2 to 10 km, and appear to concentrate at about 2–3 km. There does not seem to be any significant trend in the locations.

### 7 Focal mechanisms

Because of the large number of stations employed in this study, focal mechanisms can be obtained for individual aftershocks. This allows a more detailed examination of aftershock tectonics than is possible from construction of composite fault-plane solutions.

The velocity model used for the locations has an upper layer 3 km thick overlying a half-space. Thus earthquakes with depths less than 3 km lie above the refractor in the model. If the velocity model is not exactly correct, then rays which are refracted in the model may correspond to direct rays in the real Earth, or vice versa. The production of focal mechanisms requires the projection of an arrival back to the focal sphere, and if the ray-path is in error then the focal mechanism is incorrect. As the upper part of the velocity model is not tightly constrained, events with depths less than 3 km have not been used to obtain focal mechanisms. Thus in all the mechanisms presented here, all rays are direct rays rather than rays refracted along an interface.

Errors in the location of an earthquake will produce errors in the projection of the stations on to the focal sphere. Vertical errors in location affect the inclination of the ray-path from the source to the station, whereas horizontal errors affect both the inclination and the azimuth. Distant stations are least affected by location errors, i.e. their point of projection on to the focal sphere changes very little if the hypocentre position is moved. Shallow earthquakes are more prone to errors in inclination than are deeper earthquakes. For a horizontal location error of 1 km, and vertical error of 2 km, the error in projection position is  $<10^\circ$  of azimuth (for stations at  $>6$  km epicentral distance) and  $<12^\circ$  of inclination (if the earthquake is at  $>6$  km depth). (These figures are for a half-space velocity model.) These estimates provide only general error limits on the focal mechanisms since in any specific case the errors depend on the distribution of stations in the focal sphere. For this reason all first-motion readings for the focal mechanisms are shown in the Appendix; the parameters of the focal mechanisms are listed in Table 3. The same mechanisms are



**Table 3.** Parameters of the 81 fault-plane solutions shown in the Appendix. (Hypocentre parameters for all of the aftershock locations may be found in Ouyed 1981.)

No.	Date	Origin time	La. °N	Lo. °E	Depth (km)	Mag	Pole 1 Az Dip	Pole 2 Az Dip	P Axis Az Dip	T Axis Az Dip
29	801017	16:32	36.247	1.480	7.52	2.7	30 10	124 30	168 14	70 28
43	801018	10:23	36.207	1.489	6.74	2.8	58 10	322 20	12 20	282 6
108	801021	21:32	36.156	1.399	10.61	2.3	40 50	140 10	352 24	104 42
110	801021	22:47	36.227	1.636	6.35	2.9	17 42	132 24	344 10	80 50
122	801022	16:06	36.203	1.471	9.00	3.2	200 30	304 30	162 0	252 46
126	801022	22:38	36.215	1.462	11.20	2.7	20 10	116 35	162 20	60 30
161	801024	15:37	36.297	1.579	6.89	2.8	258 40	356 15	312 40	210 18
167	801024	21:59	36.107	1.386	6.69	3.7	350 35	118 40	158 12	56 50
169	801024	23:31	36.271	1.567	5.60	3.6	142 40	276 40	304 0	214 66
171	801025	4:23	36.207	1.511	4.65	3.3	360 25	114 40	150 10	48 50
176	801025	17:05	36.165	1.462	4.97	2.7	348 42	120 35	328 8	62 60
179	801025	23:34	36.203	1.461	8.08	3.2	146 40	288 40	288 0	212 70
183	801026	2:54	36.330	1.622	5.38	3.0	358 40	142 42	160 6	63 74
186	801026	5:54	36.243	1.647	5.99	3.0	186 15	297 60	348 28	218 54
191	801026	13:11	36.228	1.505	4.40	2.5	88 20	342 40	298 12	40 42
194	801026	17:24	36.260	1.648	5.91	2.5	14 42	140 32	348 5	82 60
198	801027	3:36	36.376	1.637	5.99	2.5	334 30	146 60	152 16	354 80
205	801027	22:12	36.065	1.366	7.77	3.5	266 25	360 10	318 30	222 12
212	801028	10:26	36.253	1.647	8.35	2.4	11 30	128 40	158 10	62 56
214	801028	13:07	36.079	1.353	6.30	3.0	22 10	290 10	340 14	64 0
217	801028	20:09	36.357	1.632	5.96	3.0	62 10	331 0	110 8	18 10
221	801029	2:01	36.365	1.621	5.66	2.3	62 15	330 0	108 10	16 12
225	801029	8:51	36.200	1.654	5.72	2.2	16 30	132 34	165 5	74 50
226	801029	12:00	36.226	1.700	9.31	2.4	22 30	125 20	345 10	76 38
240	801030	11:30	36.266	1.555	7.05	3.0	154 60	280 20	120 22	252 55
244	801030	15:40	36.306	1.540	8.65	2.6	348 40	128 40	148 0	58 66
250	801031	1:35	36.221	1.513	7.91	3.3	4 30	244 40	312 56	216 5
256	801031	11:23	36.220	1.510	7.27	2.4	268 35	26 35	330 54	240 0
259	801031	14:41	36.364	1.624	6.28	3.3	60 15	326 0	106 10	14 12
263	801031	20:02	36.229	1.705	7.40	2.6	27 30	152 44	184 10	82 60
264	801031	20:51	36.225	1.507	7.64	3.1	150 34	12 45	10 4	76 64
265	801031	21:00	36.323	1.627	3.55	3.5	8 46	144 32	348 8	82 64
273	801101	7:45	36.036	1.385	6.15	3.4	266 30	360 10	318 30	218 18
274	801101	7:52	36.037	1.385	6.19	2.6	264 30	358 10	318 28	220 12
276	801101	10:33	36.132	1.400	5.00	2.6	340 46	104 30	310 10	52 60
288	801102	3:27	36.382	1.633	6.21	2.8	350 20	107 50	142 12	40 50
290	801102	5:09	36.227	1.465	5.76	3.1	214 25	326 40	4 12	266 50
291	801102	5:21	36.338	1.633	6.91	3.9	262 5	348 0	216 4	306 4
292	801102	8:53	36.322	1.618	5.09	2.9	258 5	160 40	110 24	218 36
297	801102	15:56	36.029	1.295	13.44	4.1	324 30	88 40	118 5	28 56
301	801102	17:51	36.366	1.638	5.22	3.4	106 40	360 20	148 12	48 46
302	801102	19:25	36.292	1.576	7.46	3.0	262 40	176 0	314 30	210 28
313	801103	7:21	36.223	1.702	9.84	3.5	25 30	126 20	347 10	80 38
317	801103	11:40	36.068	1.384	7.18	3.4	32 10	298 20	350 20	258 6
324	801103	20:36	36.370	1.660	5.98	2.8	26 30	143 40	177 8	78 54
338	801104	9:16	36.245	1.635	5.11	3.7	18 30	131 34	173 6	70 50
343	801104	16:29	36.144	1.450	7.01	3.3	215 20	302 6	168 10	260 18
344	801104	17:40	36.123	1.458	7.96	3.1	196 30	298 20	155 5	248 36
345	801104	17:50	36.121	1.384	8.54	2.9	358 30	120 40	150 5	57 50
351	801105	3:00	36.207	1.496	5.14	2.1	206 30	310 36	164 6	260 46
357	801105	12:32	36.341	1.632	6.68	2.8	264 6	352 0	218 2	310 6
363	801105	20:17	36.085	1.395	9.07	2.6	358 10	264 30	318 25	220 10
366	801106	3:18	36.253	1.668	4.87	2.4	158 20	282 60	322 24	190 60
374	801106	17:21	36.365	1.614	5.30	2.9	68 25	336 0	115 18	20 20
377	801106	19:59	36.071	1.382	8.10	3.1	160 30	318 60	336 18	172 74
378	801106	22:47	36.166	1.454	6.33	3.6	356 26	140 60	164 20	30 68
387	801107	15:00	36.317	1.563	6.15	3.0	54 30	160 40	102 45	202 12
390	801107	17:47	36.363	1.665	6.40	3.1	245 20	348 40	295 45	30 14
395	801107	23:45	36.316	1.696	5.75	3.2	332 70	108 12	305 30	88 56
400	801108	4:40	36.213	1.509	5.42	3.5	150 40	288 40	130 0	220 66
404	801108	7:54	36.139	1.400	6.07	5.1	320 60	130 28	316 15	122 75
415	801109	10:50	36.130	1.411	8.32	3.3	152 24	274 50	310 16	200 58
423	801110	2:47	36.372	1.638	8.29	3.5	179 42	305 40	150 0	239 56
427	801110	6:36	36.127	1.391	5.91	2.8	340 50	118 30	322 10	66 64
428	801110	7:22	36.360	1.633	5.70	3.3	68 10	366 0	293 10	25 20
429	801110	7:24	36.229	1.514	7.39	3.2	14 30	134 40	164 4	72 54
431	801110	8:20	36.231	1.498	6.15	2.8	344 30	90 20	308 8	40 40
432	801110	9:02	36.377	1.638	6.30	3.4	358 22	109 40	146 12	48 46
434	801110	10:43	36.015	1.350	8.44	3.3	8 10	274 10	322 12	230 4
437	801110	14:39	36.126	1.404	8.27	3.5	358 86	125 40	160 8	66 52
441	801110	21:08	36.124	1.394	8.76	3.9	346 46	102 24	312 14	54 52
450	801111	20:32	36.157	1.435	7.61	3.6	198 20	298 20	148 10	252 48
453	801112	8:30	36.286	1.506	8.87	2.6	162 40	298 40	144 0	232 68
457	801112	23:16	36.272	1.561	5.33	2.6	6 10	104 30	148 10	54 28

Table 2 – continued

465	801114	2:01	36.228	1.625	5.94	2.1	12	42	130	30	343	5	76	55
467	801114	7:33	36.144	1.437	7.47	2.5	220	20	312	10	172	8	266	20
476	801114	19:14	36.235	1.489	10.03	2.5	350	65	132	20	328	25	110	60
479	801115	:12	36.227	1.678	6.77	4.0	14	48	128	20	338	14	82	52
480	801115	5:43	36.209	1.489	6.20	3.0	228	10	326	40	8	12	268	44
482	801115	6:58	36.244	1.696	8.00	3.2	172	52	342	38	163	10	333	80
492	801116	4:07	36.228	1.550	6.99	2.4	150	30	275	50	304	10	204	63

plotted on maps and sections (Figs 12–16), and these are now presented in the same sequence as the epicentral locations. The interpretations are discussed in Section 9 and shown in Figs 18–21; it may be helpful to refer to these figures in conjunction with the following paragraphs.

### 7.1 SOUTHERN SEGMENT OF FAULT BREAK

The focal mechanisms are shown in plan form and in section (Fig. 12). Two main groups can be distinguished:

(a) Eleven thrust solutions (with a minor strike-slip component). Nine of these are in a dense group at the extreme SW end of the fault breaks, and two further NE. These are all consistent with NW–SE compression.

(b) Four strike-slip solutions, approximately in the middle of the southern segment. The trend of this group is NW–SE; if this outlines the alignment of the faulting then a dextral tear fault perpendicular to the main thrust is indicated. Such faulting is observed in the surface breaks (see Fig. 1) – a dextral tear fault about 1 km long occurs above the main thrust, in the middle of the southern segment of the thrust fault.

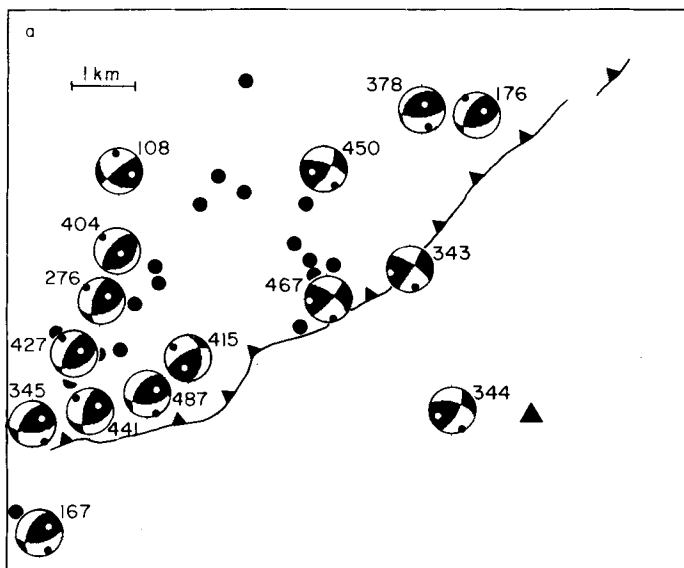


Figure 12. Map (a) and section (b) showing focal mechanisms for aftershocks of the southern segment of the fault. Mechanisms are lower hemisphere in the map and back hemisphere in the cross-section. Compressional quadrants in the focal mechanisms are shaded black, and *P*- and *T*-axes are marked by black and white dots respectively. The mechanisms are plotted on the diagrams at the locations of the relevant earthquakes. (c) shows the areas covered by the maps in Figs 12–16. The lines of the sections are the same as in Figs 7–11, and are shown in Fig. 6.

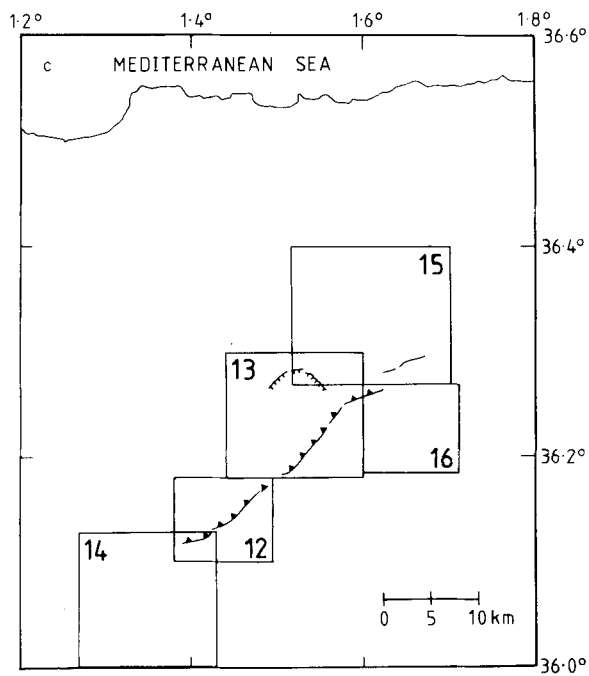
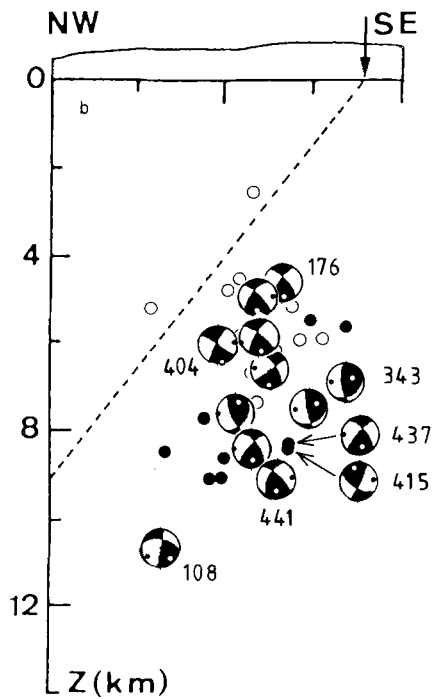
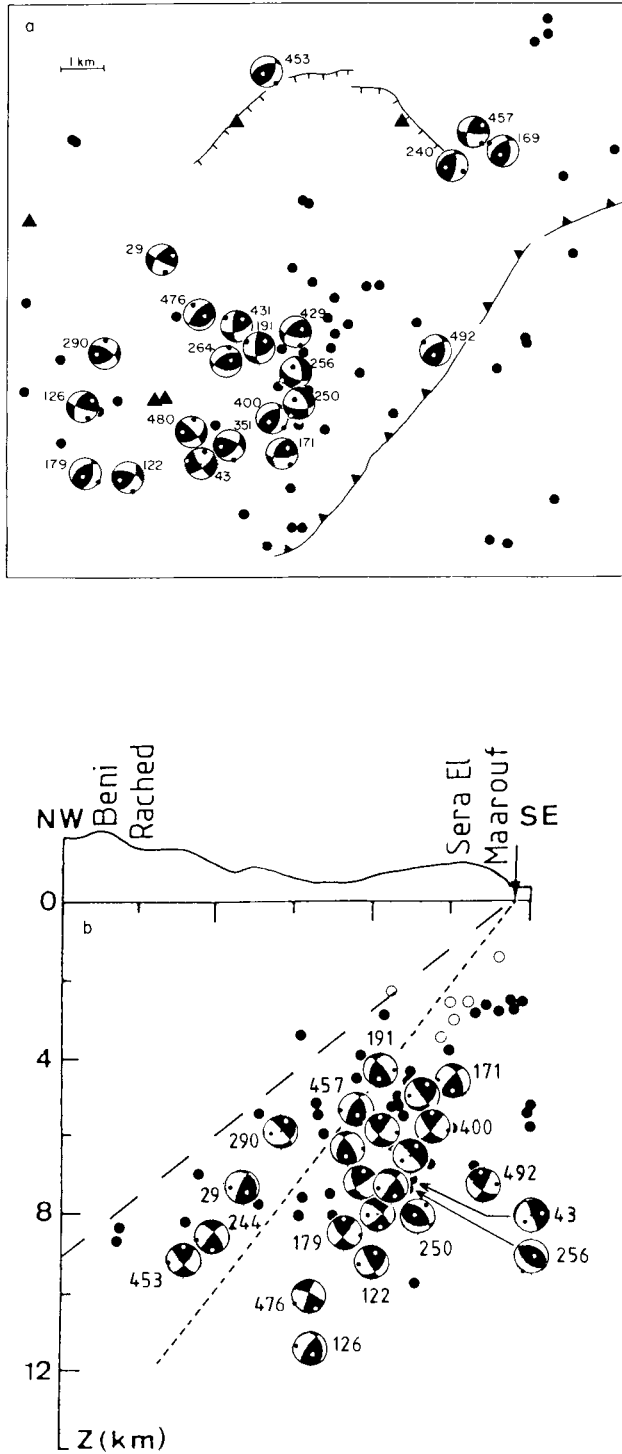


Figure 12 – continued



**Figure 13.** Map (a) and section (b) showing focal mechanisms for aftershocks of the central segment of the fault. Mechanisms are lower hemisphere in the map and back hemisphere in the cross-section. See Fig. 12(c) for location of map area.

7.2 CENTRAL SEGMENT OF FAULT BREAK

A map and section are shown in Fig. 13. Most of the solutions show thrusting (NW–SE compression). At the SW end there are a number of strike-slip solutions. These do not show a clear spatial trend (which may be a consequence of poor location accuracy), and could be due either to sinistral movement on NE–SW planes, or dextral movement on NW–SE planes. The solutions retain their strike-slip character even when recomputed at a

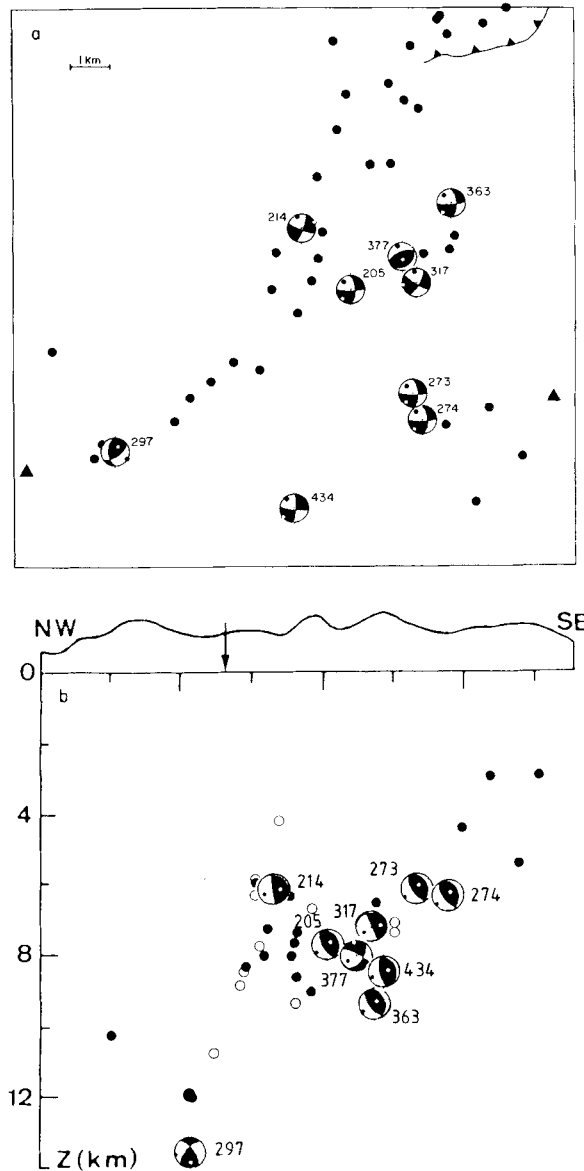


**Figure 14.** Map (a) and section (b) showing focal mechanisms for aftershocks in the area SW of the surface breaks. Mechanisms are lower hemisphere in the map and back hemisphere in the section. See Fig. 12(c) for location of map area.

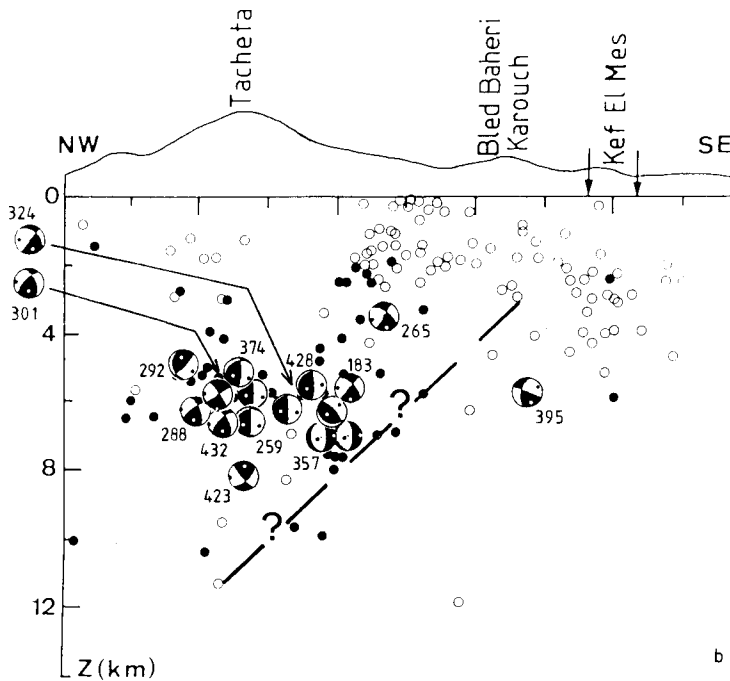
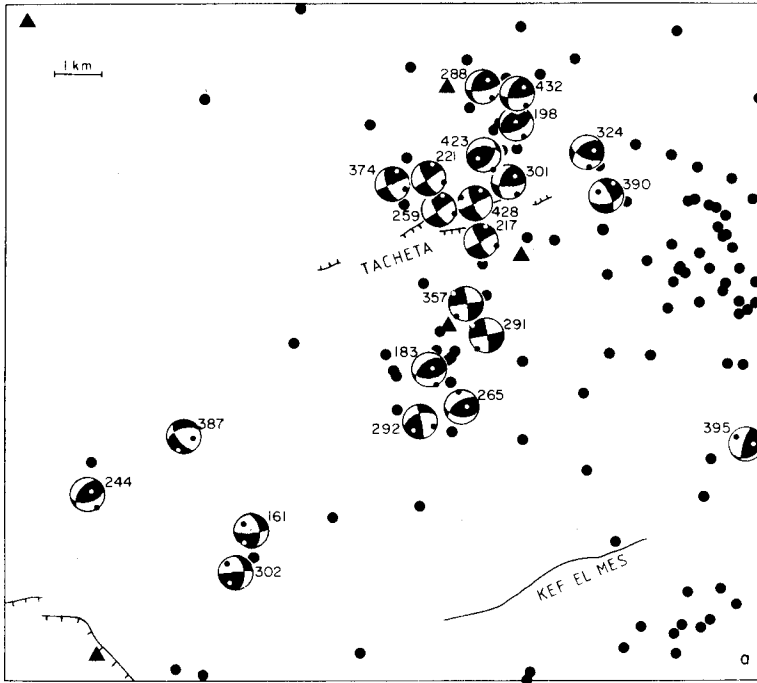


**Figure 15.** Map (a) and section (b) showing focal mechanisms for aftershocks in the north-eastern area. Mechanisms are lower hemisphere in the map and back hemisphere in the section. See Fig. 12(c) for location of map area.

variety of fixed focal depths: hence possible lack of depth control does not change the interpretation of these aftershocks as strike-slip events. These mechanisms are further discussed in Section 9. Two normal solutions (250, 256) occur towards the bottom of the cloud of events, and indicate NE–SW extension, parallel to the strike of the main fault.

### 7.3 SOUTH-WEST OF THE FAULT-BREAKS

A map and section are shown in Fig. 14. Two clear groups of solutions occur:

(a) Seven solutions are almost pure strike-slip, with N–S and E–W nodal planes, and *P*-axes oriented NW–SE. They occur over a wide area with no simple trend, even allowing for location errors. The faulting associated with these strike-slip events may be sinistral (on N–S planes) or dextral (on E–W planes), or both.

(b) Two events show thrusting (NW–SE compression) (nos 297, 377). These lie at the two ends of a NE–SW cloud of activity, extending further west than the strike-slip faulting. In section the activity is seen to lie in a NW-dipping zone. This may indicate another segment of NE-trending reverse faulting, offset to the south from the observed surface breaks.

### 7.4 NORTH-EASTERN AREA

A map and section are shown in Fig. 15. A large number of strike-slip solutions occur in the western part of this area (at the eastern end of Djebel Tacheta), forming two groups with opposite senses of movement. The smaller group (events 357 and 291) is anomalous in that the *P*-axes are aligned NE–SW and the *T*-axes NW–SE, i.e. the opposite to that expected from a NW–SE compression. No strike-slip features are known at the surface in the areas where these two groups of events occur. The strike-slip events are closely associated with thrusting solutions, the nodal planes of which tend to strike rather more easterly than the NE trends in the central and southern segments. The magnitude 5 event on 1980 October 30, and its aftershocks, occurred beneath Djebel Hangout and appear to be very shallow (<3 km, see Fig. 10); hence focal mechanisms have not been computed because of the large probable errors. Because of the scatter in the depths, it is difficult to associate the deeper thrust events with particular surface features.

### 7.5 EASTERN AREA (CHELIF VALLEY)

Focal mechanisms for this area are shown in the map and NW–SE section in Fig. 16. All the mechanisms indicate thrusting, with a greater or lesser component of strike-slip (the sense of strike-slip motion is the same in most of the events). The *P*-axes tend to be aligned more N–S than the NW–SE trends observed along the central and southern segments of the fault breaks.

## 8 Pressure and tension axes

The *P*- and *T*-axes of all the focal mechanisms are shown on a lower hemisphere plot in Fig. 17. The mean *P*-axis has an azimuthal trend of 146°, plunging 5° to the NW. This value for the mean compression direction agrees well with that of 140° from the fault-plane solution of the main shock (Ouyed *et al.* 1981). Field measurements indicated that the mean horizontal slip vector also had an azimuth of 140° (King & Vita-Finzi 1981) (the main shock was a pure thrust). The position of the pole of rotation between the African and Eurasian

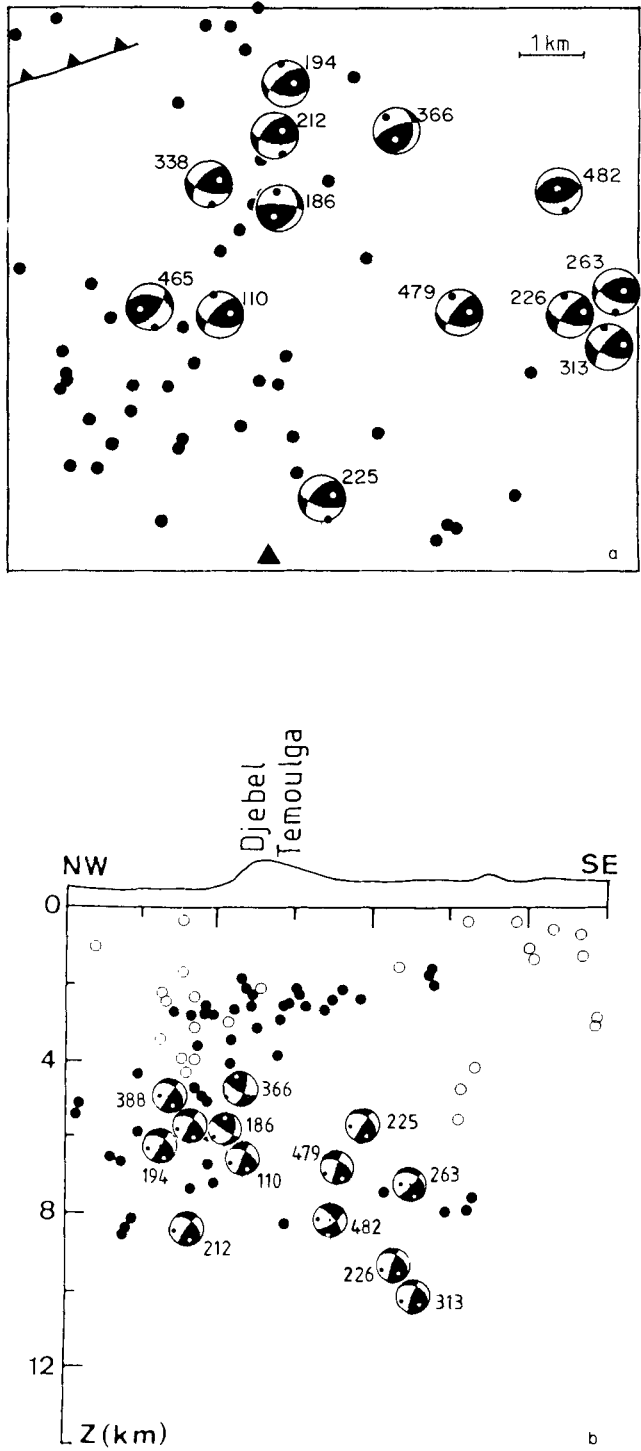


**Figure 16.** Map (a) and section (b) showing focal mechanisms for aftershocks in the eastern area (Chelif valley). Mechanisms are lower hemisphere in the map and back hemisphere in the section. See Fig. 12(c) for location of map area.



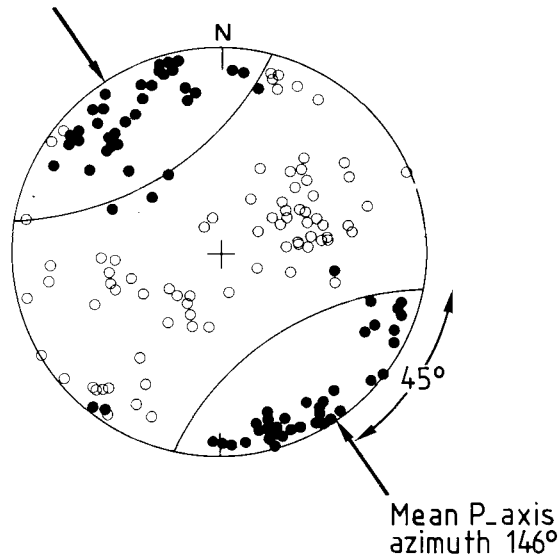


**Figure 17.** Lower hemisphere equal-area plot of the  $P$ - and  $T$ -axes for all the focal mechanisms.  $P$ -axes are shown as solid circles,  $T$ -axes as open circles. The mean  $P$ -axis is inclined upwards at  $5^\circ$  towards an azimuth of  $146^\circ$ .

plates (Minster & Jordan 1978) implies a convergence direction of  $158^\circ$  in the El Asnam area. Thus the strain relieved by the main event and its aftershocks is compatible with the compression caused by plate motion.

The scatter of  $P$ -axes about their mean (Fig. 17) does not generally exceed  $45^\circ$ . The  $T$ -axes form a girdle of points perpendicular to the mean  $P$ -axis. Within this girdle, there are two clusters, to the NE and SW of the vertical position, indicating that most of the thrust solutions have a small strike-slip component (the  $T$ -axis of a pure thrust is vertical).

## 9 Discussion

Using an array of up to 28 seismic stations, almost 500 aftershocks have been located. The best 277 of these locations have been used to examine the three-dimensional distribution of seismicity in the period 5–37 days after the main shock.  $S$ -arrivals have not been used, but it is hoped that the large number of stations will help offset the inaccuracy this introduces. The locations are believed to be accurate to  $\pm 2$  km in both epicentre and depth. Individual focal mechanisms have been obtained for 81 aftershocks.

The aftershock zone extends for about 75 km in the NE–SW direction (more than twice the length of the surface thrust break). This may be compared with the 1971 San Fernando earthquake where the aftershock zone is 50 per cent longer than the surface faulting (Whitcomb *et al.* 1973), and the 1978 Tabas (Iran) earthquake where the aftershock activity does not extend beyond the ends of the mapped surface breaks (Berberian 1982). The complexity seen in the pattern of surface faulting is reflected in the distribution of aftershocks. Clusters of aftershocks occur beneath the central and southern segments of the main thrust break. The abundance of aftershock activity is greatest to the NE, where normal faulting on anticlinal ridges was widespread after the main shock.

Along the central and southern segments, the surface faulting and geological structures indicate a single NW-dipping reverse fault (King & Vita-Finzi 1981; Ouyed *et al.* 1981;

Yielding *et al.* 1981). However, the aftershocks do *not* define a simple fault zone dipping NW from the observed surface break. Instead they seem to be clustered in the footwall of the fault, with little or no seismic deformation in the hanging-wall. This is particularly clear for the southern segment (Fig. 7), and is probably true for the central segment if a shallower fault dip [implied by waveform modelling (Yielding *et al.* 1981)] is assumed. Although the aftershocks of strike-slip earthquakes are often observed to lie along the mainshock fault-plane (e.g. Eaton, O'Neill & Murdoch 1970; Ellsworth 1975), aftershocks of normal and thrust earthquakes typically indicate movement either on neighbouring faults or within the blocks adjacent to the main fault [documented examples include the 1971 San Fernando earthquake (Whitcomb *et al.* 1973), the 1976 Friuli earthquake (Cagnetti & Pasquale 1979), the 1978 Thessaloniki earthquake (Soufleris *et al.* 1982), and the 1978 Tabas-e-Golshan earthquake (Berberian 1982)]. The footwall deformation occurring after the El Asnam earthquake was dominantly compressive. Focal mechanisms indicate thrusting on NE–SW planes, similar to that observed in the main shock. Focal mechanisms alone do not distinguish between the fault planes and the auxiliary planes, so these aftershocks may have occurred either on NW-dipping planes (parallel to the main fault), or on SE-dipping planes (conjugate faulting). These two possibilities are illustrated in Fig. 18. Conjugate thrust faults (as in Fig. 18b) have been identified (using COCORP reflection data) beneath the Wind River Thrust of Wyoming (Brewer *et al.* 1980; Zawislak & Smithson 1981), which is of comparable size to the reverse fault which ruptured in the El Asnam main shock.

Focal mechanisms of aftershocks NE and east of the main surface breaks also indicate thrusting as the dominant type of faulting. However, the northward-dipping nodal planes of these focal mechanisms tend to have a more easterly trend than the aftershocks of the central and southern fault segments. This is consistent with the more easterly trend of the anticlinal ridges seen at the surface in this area (Fig. 1). The predominance of thrusting confirms the earlier interpretation (Yielding *et al.* 1981) that the anticlinal ridges and their associated tensional surface breaks are underlain by major northward-dipping reverse faults. None of the focal mechanisms obtained in this study are consistent with normal faulting on NE-trending planes, implying that the normal faulting observed after the main shock was not seismogenic. This strongly suggests that the normal faulting observed at the surface is a shallow feature caused by tension on the top of anticlines, as proposed by King & Vita-Finzi

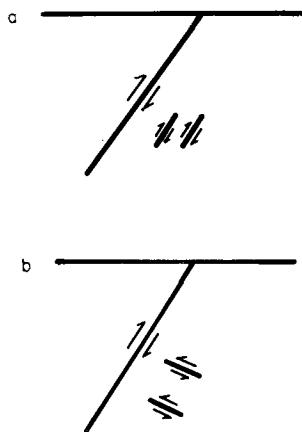


**Figure 18.** Cartoon illustrating two possible interpretations of thrusting in the footwall of the main thrust fault: (a) minor faults parallel to the main fault; (b) conjugate thrust faults.

(1981). The Beni Rached area was almost devoid of aftershocks, and the few which occurred are associated with the deeper part of the central segment of the main thrust (see Fig. 8). It is therefore probable that the Beni Rached surface breaks were caused by movement of a large south-directed landslip.

Although the majority of the focal mechanisms of the aftershocks indicate thrusting caused by NW–SE compression, a significant proportion indicate strike-slip faulting. These fall into two main groups. The first group is characterized by N–S and E–W nodal planes, with  $P$ -axes aligned NW–SE. These mechanisms could be caused by a system of conjugate strike-slip faulting, which would take up the same NW–SE shortening as the thrusting: Fig. 19(a) shows schematically such a system of faults, and the focal mechanisms that would be produced.

The second type of strike-slip faulting is characterized by NE–SW and NW–SE nodal planes, with  $P$ -axes oriented either N–S or E–W. This is a different orientation of  $P$ -axis to that indicated by the thrusting. However, if the NW–SE nodal planes were always the fault planes, then the horizontal slip vectors would be parallel to the horizontal slip vector of the thrusting. This motion is geometrically consistent with NW–SE convergence. Fig. 19(b) indicates schematically how such strike-slip faulting can result from motion on a segmented thrust fault. Dextral and sinistral faulting can occur along the edges of the blocks which move forwards along thrust planes. [Note that Fig. 19(b) is *not* a representation of part of the El Asnam fault system, but is intended to show how thrust and strike-slip faulting can be related geometrically.]

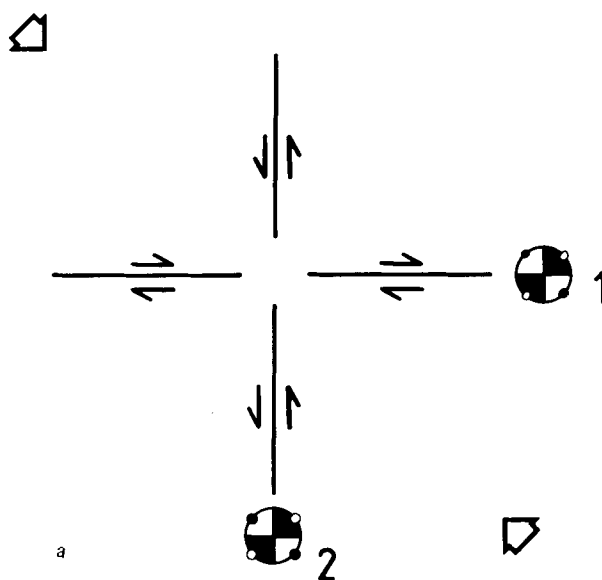


**Figure 19.** (a) Cartoon illustrating fault-plane solutions on a conjugate strike-slip fault system, with NW–SE compression. (b) Cartoon illustrating fault-plane solutions on a thrust fault bounded by geometrically controlled strike-slip faults. (Note that this cartoon is not intended to represent a specific part of the El Asnam fault system.) (c) Lower hemisphere equal-area plot of  $P$ - and  $T$ -axes from the numbered fault-plane solutions shown in (a) and (b). Note that  $P$ -axes deviate by up to  $45^\circ$  from the mean compression direction, and that the  $T$ -axes form a girdle perpendicular to the mean compression direction. Note also the similarity of this plot to Fig. 17.

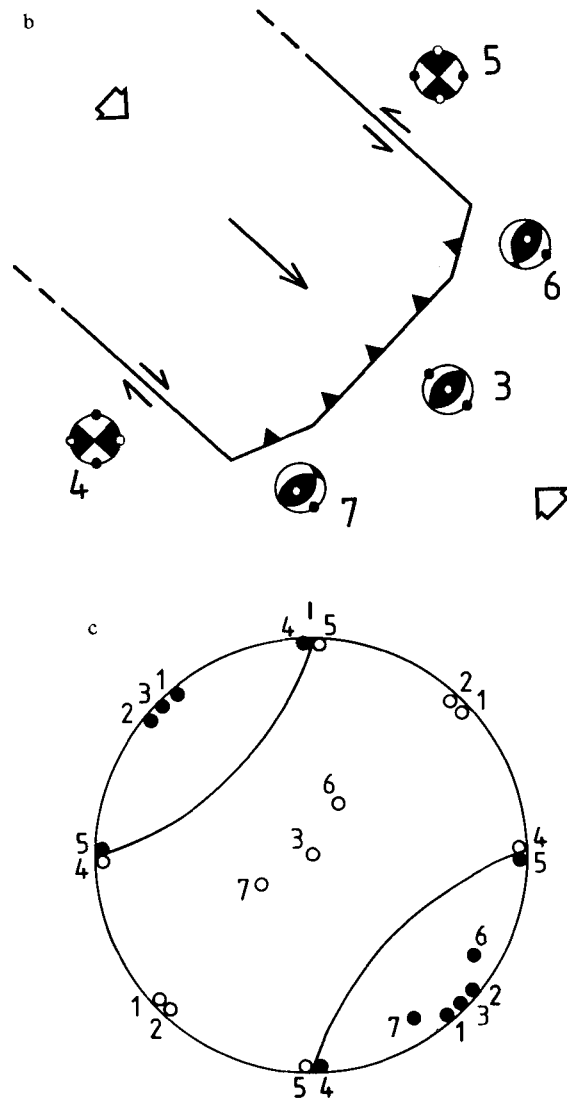
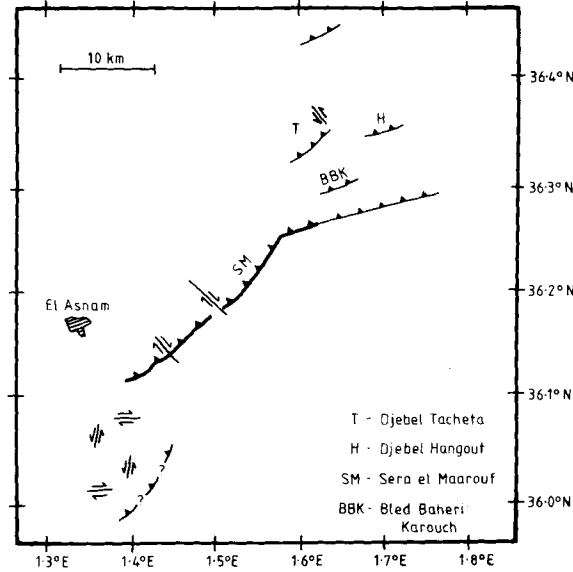


Figure 19 – continued

Fig. 19(c) shows a lower hemisphere plot of the  $P$ - and  $T$ -axes for the various theoretical focal mechanisms shown in Figs 19(a) and (b).  $P$ -axes cluster along the direction of maximum compression. However, some  $P$ -axes may deviate from this direction by  $45^\circ$ , and these correspond to the fault-plane solutions of strike-slip faulting on NW–SE planes (mechanisms 4 and 5 in Fig. 19b).  $T$ -axes occupy a broad girdle, generally aligned perpendicular to the direction of maximum compression, but reaching to within  $45^\circ$  of it. The observed pattern of  $P$ - and  $T$ -axes for the El Asnam aftershocks (Fig. 17) is very similar to that in Fig. 19(c), implying that the NW–SE compression could be accommodated by a combination of mechanisms, namely thrusting, conjugate strike-slip faulting, and geometrically controlled strike-slip faulting.



**Figure 20.** Schematic map showing the tectonics of the aftershock zone, based on aftershock focal mechanisms, surface faulting, geological structures and morphology. The thick barbed line represents the main fault break, the thin barbed lines represent other faults. In the SW area we show two alternative interpretations of the seismicity (conjugate strike-slip faulting, or another reverse fault offset to the south). Note the greater complexity of faulting at both ends of the main shock surface break.

Geometrically related strike-slip faulting and thrusting have been recognized in other earthquake sequences. Following the 1971 San Fernando earthquake (on an ESE-trending thrust fault), a large proportion of the aftershocks occurred on a NNE-trending sinistral tear fault at one end of the thrust block (Whitcomb *et al.* 1973). The 1968 Dasht-e-Bayaz earthquake occurred on an E–W strike-slip fault, but some of the major aftershocks indicated thrusting near the termination of the main fault (Jackson, Fitch & McKenzie 1981). The 1974 Markansu Valley earthquake sequence also involved both thrusting (on planes trending E–W) and strike-slip faulting (on planes trending N–S and NW–SE) (Jackson *et al.* 1979, 1981).

The detailed nature of the seismic deformation changes along the length of the fault zone. Fig. 20 is an interpretative map showing the inferred pattern of faulting involved in the aftershocks. At the SW end of the aftershock zone, conjugate strike-slip faulting appears to occur. A system consisting only of conjugate strike-slip faults (as in Fig. 19a) is geometrically impossible if finite motion occurs. For such conjugate faulting to exist it is necessary that small-scale adjustment takes place near the ends of the faults or where the faults would intersect. This could take the form of motion on smaller faults, or elastic or plastic deformation in the medium. Two thrusting mechanisms also occur in this area (see Fig. 14), and in cross-section the activity appears to define a simple NW-dipping zone. Hence an alternative interpretation for the seismicity of the south-western area is that there is another segment of reverse faulting, offset to the south from the observed surface breaks.

Along the southern segment of the observed fault break, deformation is primarily by compression in the footwall of the main fault. In addition, a NW-trending dextral tear fault splits the southern segment into two. The tear faulting is observable seismically in the footwall, and seen as surface breaks in the hanging wall.

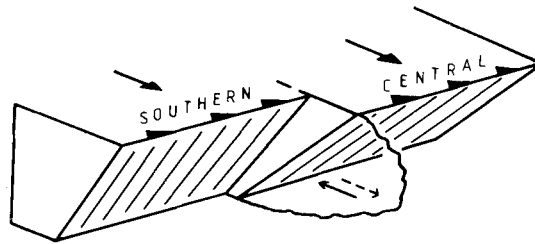


**Figure 21.** Diagram illustrating the possible nature of the offset between the southern and central segments of the main fault. Many compressional aftershocks occur in the footwall of the central segment, but strike-slip aftershocks are observed at its SW end. It appears that the lateral offset between the thrust segments is extending into the footwall. Such extension is to be expected as a consequence of the greater amount of seismic activity in the footwall NE of the offset.

Along the central segment of the observed fault break, most of the deformation is also confined to the footwall of the main fault. It seems that the dip of the main fault is shallower here ( $40\text{--}45^\circ$ ) than it is along the southern segment ( $50\text{--}60^\circ$ ). The SW end of the central segment is marked by strike-slip faulting, caused by south-eastwards movement in the central segment. A cartoon illustrating the possible nature of the junction between the southern and central segments is shown in Fig. 21. The cross-section of the central segment (see Fig. 13) suggests that the strike-slip faulting is occurring well forward (SE) of the main thrust faults. This requires that the dextral motion is between the footwall of the central segment and the footwall of the southern segment, as shown in Fig. 21. Such motion probably arises because there is considerably thrusting, and hence compression, in the footwall north of the junction, but relatively little activity immediately south of the junction.

In the NE area of the aftershock zone, thrusting and strike-slip faulting again occur close to one another. Here, however, the thrust faulting appears to be caused by motion on NW-dipping fault surfaces, rather than in the blocks adjacent to faults. These reverse faults were inferred by Yielding *et al.* (1981) to have undergone some displacement during or soon after the main shock, but did not break the surface. Most of the strike-slip faulting is consistent with being geometrically controlled by the reverse faulting, i.e. the solutions have one slip vector similar to the thrusting (see Fig. 15). However, because of the smaller scale of the faulting compared to that along the main thrust, the detailed relationships between the thrusting and strike-slip motion are harder to resolve in the NE area.

## 10 Conclusions

The aftershock zone of the El Asnam 1980 earthquake extended more than twice the length of the well-developed surface thrust fault, and can be divided into three areas:

(1) In the region of the central and southern segments of the fault break, which experienced substantial displacement during the main shock, most of the aftershocks indicate thrusting and are confined to the footwall of the fault. At junctions between thrust fault segments, motion appears to be taken up by strike-slip faulting. This is apparent from the fault-plane solutions and can be seen as a surface feature in one place.

(2) The large number of aftershocks in the NE area appears to be due to reactivation of a fan-like system of smaller reverse faults associated with surface folding.

(3) Activity at the SW end is considerably less than in the NE. Thrusting occurs but some deformation appears to be accommodated by conjugate strike-slip faulting. There is no apparent relation between this activity and geological or morphological features.

### Acknowledgments

We thank C. Antenor-Habazac, P. Y. Bard, M. Bouchon, A. Cisternas, J. Dorel, J. Frechet, M. Frogneux, N. Girardin, J. C. Lepine, G. Poupinet, H. Sinvhal, C. Vita-Finzi and R. M. Wood who helped to operate the seismic stations. D. Bensari (Director of SPGM, Rabat) provided instruments. H. Ferrieux and B. Mohammadioun (CEA, Paris) communicated their arrival-time data. We are greatly indebted to H. Benhallou (Director of CNAAG) and R. Abdelhalim (Director of CRAG), Algiers, for providing support in the field. We benefited from fruitful discussion with J. Frechet, and J. Jackson kindly read through the manuscript.

This research was supported by INAG (France) and NERC and the Royal Society (UK). Department of Earth Sciences Cambridge University contribution no. 367.

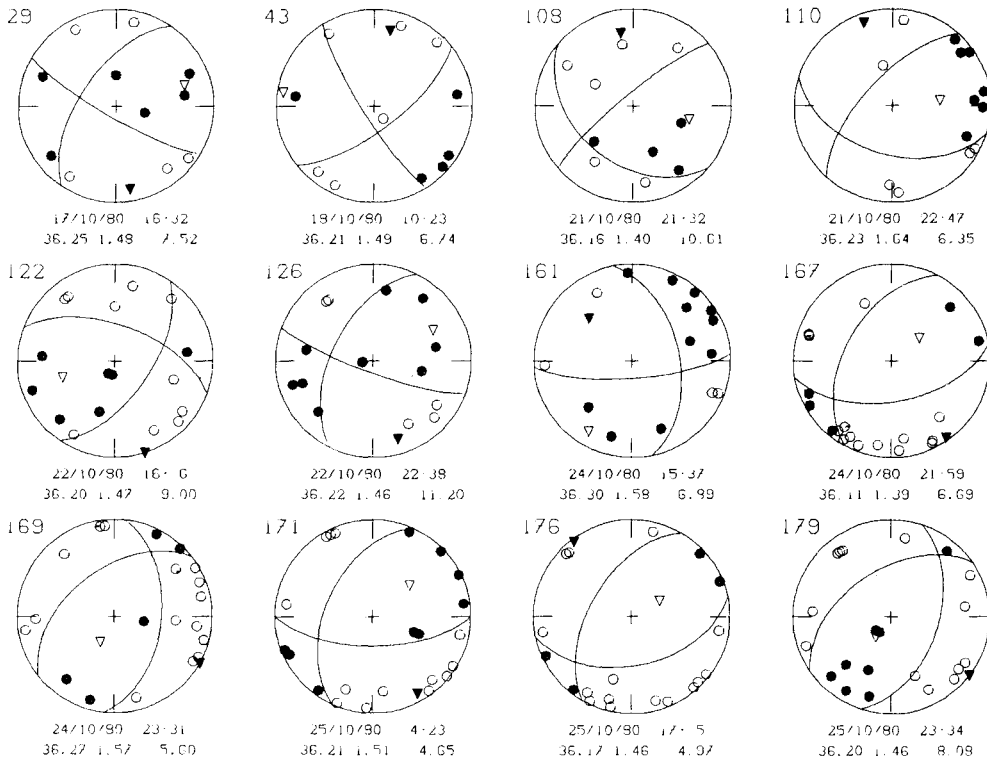
### References

- Adams, R. C., 1977. Survey of practice in determining magnitudes of near earthquakes, *World Data Center A, Rep. SE-8*.
- Ambraseys, N. N., 1981. The El Asnam earthquake of 10 October 1980; conclusions drawn from a field study, *Q. J. eng. Geol.*, **14**, 143–148.
- Berberian, M., 1982. Aftershock tectonics of the 1978 Tabas-e-Golshan (Iran) earthquake sequence: a documented active 'thin- and thick-skinned tectonic' case, *Geophys. J. R. astr. Soc.*, **68**, 499–530.
- Bockel, M., 1972. Structure de la croûte terrestre en Algérie d'après les ondes sismiques, *Annali. Geofis.*, **25**, 339–358.
- Brewer, J. A., Smithson, S. B., Oliver, J. E., Kaufman, S. & Brown, L. D., 1980. The Laramide orogeny: evidence from COCORP deep crustal seismic profiles in the Wind River Mountains, Wyoming, *Tectonophys.*, **62**, 165–189.
- Buland, R., 1976. The mechanics of locating earthquakes, *Bull. seism. Soc. Am.*, **66**, 173–187.
- Cagnetti, V. & Pasquale, V., 1979. The earthquake sequence in Friuli, Italy, 1976, *Bull. seism. Soc. Am.*, **69**, 1797–1818.
- Cisternas, A., Dorel, J. & Gaulon, R., 1982. Models of the complex source of the El Asnam earthquake, *Bull. seism. Soc. Am.*, **72**, 2245–2266.
- Deschamps, A., Gaudemer, Y. & Cisternas, A., 1982. The El Asnam earthquake of October 10, 1980; multiple source mechanism determined from long period records, *Bull. seism. Soc. Am.*, **72**, 1111–1128.
- Eaton, J. P., O'Neill, M. E. & Murdoch, J. N., 1970. Aftershocks of the 1966 Parkfield-Cholame, California, earthquake: a detailed study, *Bull. seism. Soc. Am.*, **60**, 1151–1197.
- Ellsworth, W. L., 1975. Bear Valley, California, earthquake sequence of February–March 1972, *Bull. seism. Soc. Am.*, **65**, 483–506.
- Ellsworth, W. L. & Roecker, S. W., 1983. Sensitivity of the earthquake location problem to network geometry, *Geophys. J. R. astr. Soc.*, submitted.
- Jackson, J., Molnar, P., Patton, H. & Fitch, T. J., 1979. Seismotectonic aspects of the Markansu Valley, Tadzhikistan earthquake of August 11, 1974, *J. geophys. Res.*, **84**, 6157–6167.
- Jackson, J., Fitch, T. J. & McKenzie, D. P., 1981. Active thrusting and the evolution of the Zagros fold belt, in *Thrust and Nappe Tectonics*, eds McClay, K. R. & Price, N. J., *Spec. Publ. geol. Soc. London*, No. 9, pp. 371–379, Blackwell Scientific Publications, Oxford.
- James, D. E., Sacks, I. S., Lazo, E. & Aparicio, P., 1969. On locating local earthquakes using small networks, *Bull. seism. Soc. Am.*, **59**, 1201–1212.
- King, G. C. P. & Vita-Finzi, C., 1981. Active folding in the Algerian earthquake of 10 October 1980, *Nature*, **292**, 22–26.
- Klein, F. W., 1978. Hypocenter location program HYPOINVERSE, *Open-File Rep. U. S. geol. Surv.*, **78-694**.
- Lee, W. H. K. & Lahr, J. C., 1975. HYPO71 (revised): a computer program for determining hypocenter, magnitude, and first-motion pattern of local earthquakes, *Open-File Rep., U. S. geol. Surv.*, **75-311**.
- Lepvrier, C., 1981. Le cadre structural des séismes d'El Asnam (Algérie), *C. r. hebd. Séanc. Acad. Sci. Paris*, **292**, Serie II, 113–116.
- Mattauer, M., 1963. Le style tectonique des chaînes telliennes et rifaines, *Geol. Rdsch.*, **53**, 296–313.
- Minster, J. B. & Jordan, T. H., 1978. Present-day plate motions, *J. geophys. Res.*, **83**, 5331–5354.
- Ouyed, M., 1981. Le tremblement de terre d'El Asnam du 10 Octobre 1980; étude des repliques, *Thèse de 3e cycle*, Université Scientifique et Médicale de Grenoble.

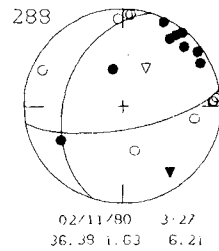
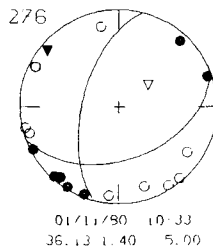
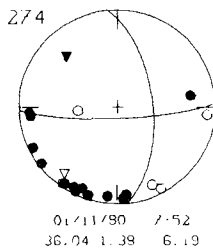
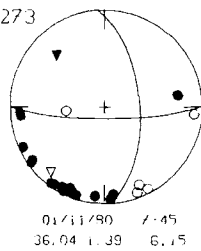
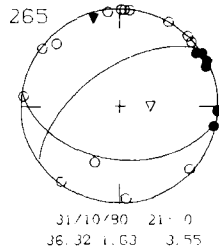
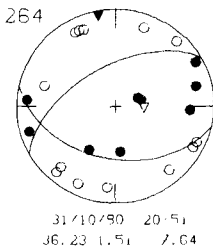
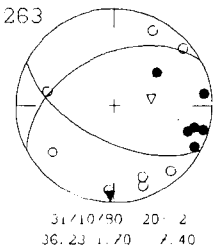
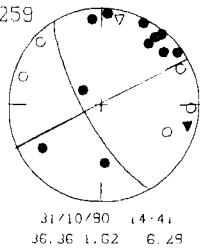
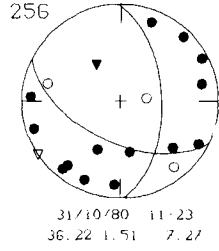
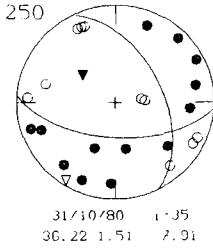
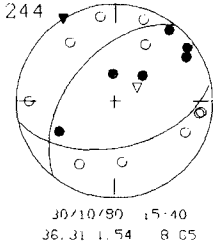
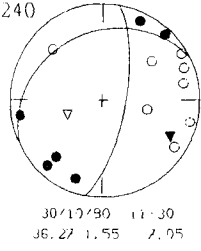
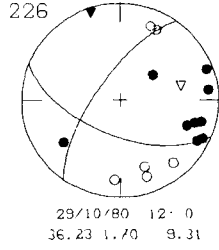
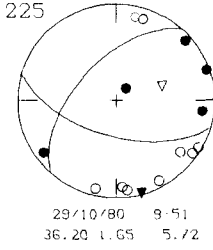
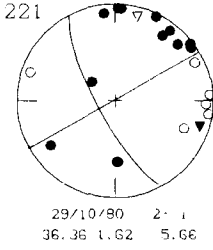
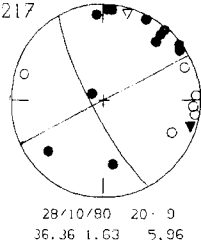
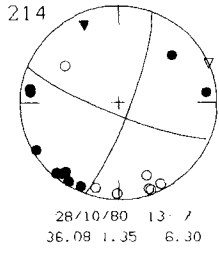
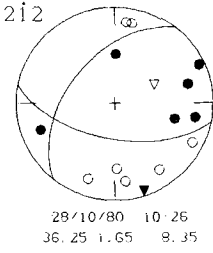
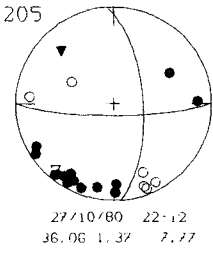
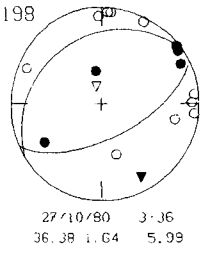
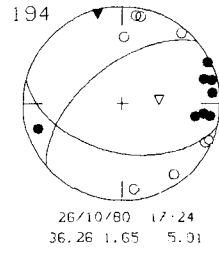
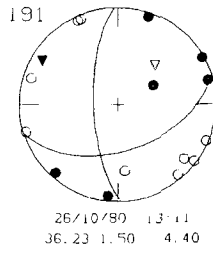
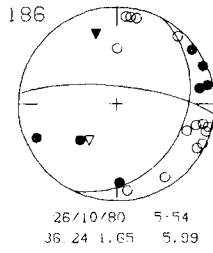
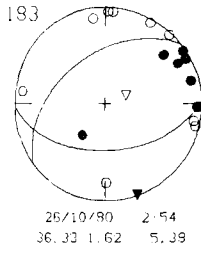
- Ouyed, M., Meghraoui, M., Antenor-Habazac, C., Bourezg, S., Cisternas, A., Dorel, J., Fréchet, J., Frogneux, M., Hatzfeld, D. & Philip, H., 1980. Le séisme d'El Asnam du 10 Octobre 1980, premiers résultats sismologiques et tectoniques, *C. r. hebd. Séanc. Acad. Sci. Paris*, **291**, Serie D, 921–924.
- Ouyed, M., Meghraoui, M., Cisternas, A., Deschamps, A., Dorel, J., Fréchet, J., Gaulon, R., Hatzfeld, D., Philip, H., 1981. Seismotectonics of the El Asnam earthquake, *Nature*, **292**, 26–31.
- Perrodon, A., 1957. Etude géologique des Bassins Neogènes sublittoraux de l'Algérie Occidentale, *Bull. Serv. Carte géol. Algér., N. Ser.*, **12**, 1–328.
- Philip, H. & Meghraoui, M., 1983. Structural analysis and interpretation of the surface deformation of the El Asnam earthquake of October 10, 1980, *Tectonics*, submitted.
- Rothé, J. P., 1955. Le tremblement de terre d'Orléansville et la sismicité de l'Algérie, *La Nature*, **3237**, 1–9.
- Sapin, M., Wittlinger, G., Hirn, A. & Djeddi, M., 1983. Local earthquakes on 3-component seismograms, in preparation.
- Soufleris, C., Jackson, J. A., King, G. C. P., Spencer, C. P. & Scholtz, C. H., 1982. The 1978 earthquake sequence near Thessaloniki, (northern Greece), *Geophys. J. R. astr. Soc.*, **68**, 429–458.
- Whitcomb, J. H., Allen, C. R., Garmany, J. D. & Hileman, J. A., 1973. San Fernando earthquake series, 1971: focal mechanisms and tectonics, *Rev. Geophys. Space Phys.*, **11**, 693–730.
- Yielding, G., Jackson, J. A., King, G. C. P., Sinvhal, H., Vita-Finzi, C. & Wood, R. M., 1981. Relations between surface deformation, seismicity, rupture characteristics and fault geometry during the El Asnam (Algeria) earthquake of 10 October 1980, *Earth planet. Sci. Lett.*, **56**, 287–304.
- Zawislak, R. L. & Smithson, S. B., 1981. Problems and interpretation of COCORP deep seismic reflection data, Wind River Range, Wyoming, *Geophysics*, **46**, 1684–1701.

## Appendix

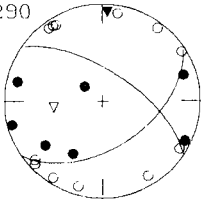
Lower-hemisphere equal-area fault-plane solutions for 81 aftershocks recorded by the portable array. Compressional first-motions are shown as solid circles, dilatational first-motions as open circles. *P*-axes are shown as solid triangles, and *T*-axes as open triangles.





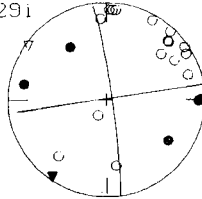


290



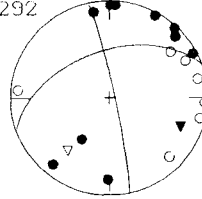
02/11/80 5.9  
36.23 1.47 5.76

291



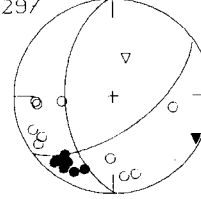
02/11/80 5.21  
36.34 1.63 6.91

292



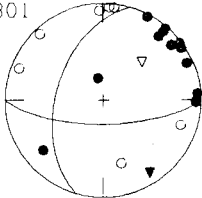
02/11/80 9.53  
36.32 1.62 5.09

297



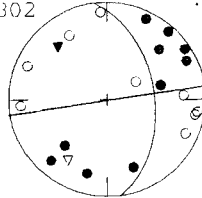
02/11/80 15.56  
36.03 1.30 13.44

301



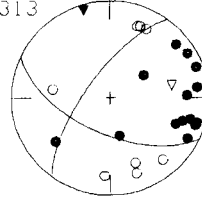
02/11/80 17.51  
36.37 1.64 5.22

302



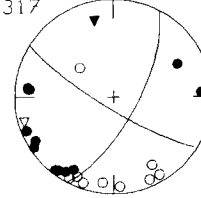
02/11/80 19.25  
36.29 1.58 7.46

313



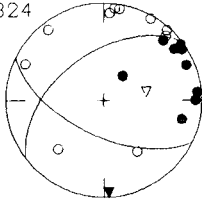
03/11/80 7.21  
36.22 1.70 9.94

317



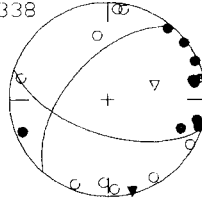
03/11/80 11.40  
36.07 1.38 7.19

324



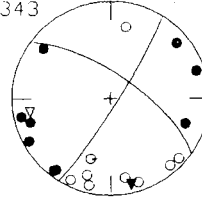
03/11/80 20.36  
36.37 1.66 5.98

338



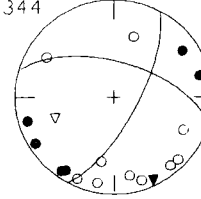
04/11/80 9.16  
36.24 1.64 5.11

343



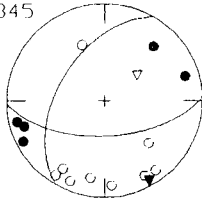
04/11/80 16.29  
36.14 1.45 7.01

344



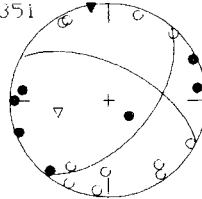
04/11/80 17.40  
36.12 1.46 7.96

345



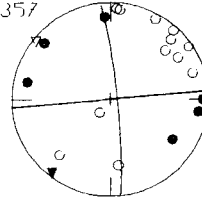
04/11/80 17.50  
36.12 1.39 9.54

351



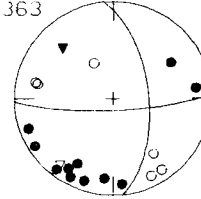
05/11/80 3.0  
36.21 1.50 5.14

357



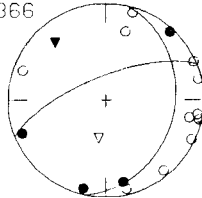
05/11/80 12.32  
36.34 1.63 6.68

363



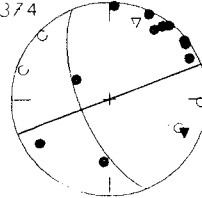
05/11/80 20.17  
36.09 1.39 9.07

366



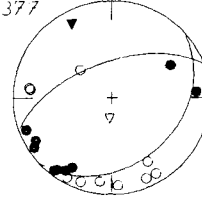
06/11/80 3.13  
36.25 1.67 4.37

374



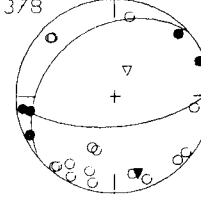
06/11/80 17.21  
36.32 1.61 5.30

377



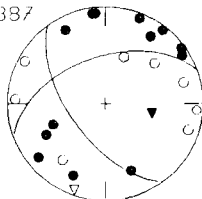
06/11/80 13.59  
36.07 1.39 9.10

378



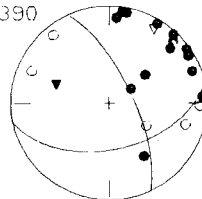
06/11/80 22.47  
36.17 1.45 6.33

387



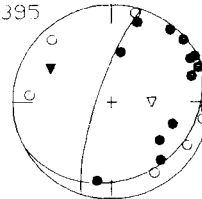
07/11/80 15.0  
36.32 1.56 6.15

390



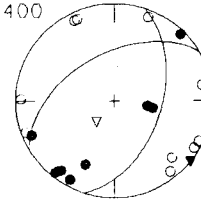
07/11/80 17.47  
36.36 1.66 6.40

395



07/11/80 23.45  
36.32 1.70 5.75

400



09/11/80 4.40  
36.21 1.51 5.42

